NACA TN 4133

NATIONAL ADVISORY COMMITTEE FOR AERONAUTICS

TECHNICAL NOTE 4133

BOUNDARY-LAYER DISPLACEMENT EFFECTS IN AIR AT MACH NUMBERS OF 6.8 AND 9.6

By Mitchel H. Bertram

Langley Aeronautical Laboratory
Langley Field, Va.

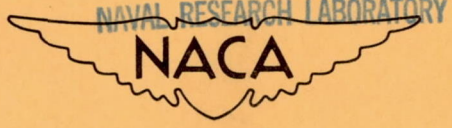

Washington
February 1958

NATIONAL ADVISORY COMMITTEE FOR AERONAUTICS

TECHNICAL NOTE 4133

BOUNDARY-LAYER DISPLACEMENT EFFECTS IN AIR AT MACH NUMBERS OF 6.8 AND 9.6

By Mitchel H. Bertram

SUMMARY

Measurements are presented for pressure gradients induced by a laminar boundary layer on a flat plate in air at a Mach number of 9.6 and for the drag of thin wings at a Mach number of about 6.8 and zero angle of attack. The pressure measurements at a Mach number of 9.6 were made in the presence of substantial heat transfer from the boundary layer to the plate surface. The measured pressure distribution on the surface of the plate was predicted with good accuracy by a modification to insulated-plate displacement theory which allows for the effect of the heat transfer and temperature gradient along the surface on the boundary-layer displacement thickness.

The total drag of thin wings with square and delta plan forms was measured at a nominal Mach number of 6.8 over a reasonably wide range of Reynolds numbers. The total drag was found to be greater than can be explained by adding a classical value of laminar skin friction to the estimated pressure drag. The difference is, in general, explained by the increase in skin friction (20 to 40 percent) caused by the boundary-layer-induced pressures.

INTRODUCTION

The considerable distortion of the flow field about plane surfaces or slender bodies in hypersonic flow due to boundary-layer displacement effects is now well known qualitatively. This phenomenon is a result of the low mass involved in laminar boundary-layer flow and can achieve considerable importance at high Mach numbers and low Reynolds numbers. The most readily observable result of the presence of the boundary layer is a local increase in surface pressure which appears in conjunction with an increase in skin friction and heat transfer. A considerable body of quantitative theoretical evaluations of this effect is now available. These solutions are concerned mainly with the sharp-leading-edge problem and can be considered to fall into two classes, the so-called

"weak interaction" and "strong interaction" solutions. Expressed rather simply, the weak-interaction regime is one in which the self-induced pressure gradient does not have an important effect on the boundary-layer growth, whereas in the strong-interaction regime large induced pressures occur which do have an important effect on the boundary-layer growth and necessitate consideration of the mutual interaction between the boundary layer and the boundary-layer-induced pressure gradients.

The parameter which basically determines the region in which interaction effects can be important was first given by Lees and Probstein (ref. 1). This parameter takes into account Mach number, Reynolds number, and temperature level of the external stream. Other evaluations of the weak- and strong-interaction regions have been made by Bertram, Shen, Li and Nagamatsu, Stewartson, Lees, Kuo, and Pai and Shen (refs. 2 to 9).

The experimental work in air has been mainly supplied by Bertram for a Mach number of 6.9 (refs. 2 and 10) and Kendall for a Mach number of 5.8 (ref. 11). The main drawback to this data taken in air has been that only the lower end of the range in which the self-induced effects become important has been explored. The data which have been obtained in helium by Bogdonoff and Hammitt at the Princeton helium hypersonic tunnel (refs. 12 and 13) cover a range in which the self-induced effects can be of major importance. Most of these helium data, however, include a considerable leading-edge-bluntness effect which makes difficult the comparison with viscous-interaction theory.

Among the boundary-layer-induced effects are the pressure gradient induced by the presence of the boundary layer and the increase in skin friction associated with this induced pressure gradient. With the recent availability of a nominal Mach number 10 nozzle for the Langley 11-inch hypersonic tunnel there was the possibility of considerably extending the range of the interaction data in air. This nozzle has been utilized to obtain new measurements of the boundary-layer-induced pressures, although heat transfer from the boundary layer to the model is present in these experimental results. These measurements are presented in this report, together with measurements of the total drag at zero lift of wings with thin square and delta plan forms in the nominal Mach number 7 nozzle of the 11-inch hypersonic tunnel. These total-drag measurements are utilized to obtain an indication of the increased skin friction that can be ascribed to the induced pressure field.

SYMBOLS

A	constant in Blasius formula for skin friction
a	fraction of root chord of delta wing

a', b' skin-friction constants in viscous-interaction theory

B second virial coefficient in equation of state for imperfect gas

b wing semispan

$C = \mu_w T_\infty / \mu_\infty T_w$

C, D constants in power formulas for turbulent skin friction in appendix D (eqs. (D12) and (D14))

$C_l = \mu_w T_l / \mu_l T_w$

$C_{D,p}$ wave- or pressure-drag coefficient at zero angle of attack

$C_{D,T}$ total drag coefficient at zero angle of attack

$C_{D,t}$ leading-edge drag coefficient based on wing area

C_F average skin-friction drag coefficient

$\overline{C_F}$ average skin-friction drag coefficient without displacement effect

C_f local skin-friction drag coefficient

$\overline{C_f}$ local skin-friction drag coefficient without displacement effect

$C_{p,max}$ pitot pressure coefficient

$C_{p,t}$ average pressure coefficient over leading edge of wing

c local chord

$\bar{c}$ effective chord of a wing for the determination of average skin friction (see appendix D, eq. (D1))

Δc length of sting contained within the wing plan form (fig. 3)

c_r root chord

d sting thickness (fig. 3)

$F \equiv 0.149(\gamma - 1)(\gamma + 1)$

f length of sting base flare (fig. 3)

g length of sting outside of wing plan form (fig. 3)

$k \equiv \frac{\gamma - 1}{2} M^2$

L plate length

M Mach number

m,n,q reciprocals of exponents in power laws for skin friction in appendix D

N_{Kn} Knudsen number, $\frac{\text{Molecular mean free path}}{\text{Leading-edge thickness}}$

N_{Pr} Prandtl number

p pressure

p_c critical pressure of gas

p_0' total pressure measured by pitot tube

R Reynolds number based on undisturbed free-stream conditions

$\overline{R}$ gas constant

R_{c_r} Reynolds number with root chord of delta wing as characteristic length

R_T Reynolds number for transition based on distance from leading edge in free-stream direction

R_t Reynolds number with leading-edge thickness as characteristic length

R_x Reynolds number with x as characteristic length

s local lateral dimension of plate or wing from center line

T absolute temperature

T_c critical temperature of gas

$T_{P,\infty}$	static temperature for constant value of γ
t	leading-edge thickness
u	velocity
X,Y,Z	nozzle coordinates (fig. 1)
x	longitudinal distance from leading edge of plate
y	distance measured laterally on model from center line
α	angle of attack
β	Sutherland constant
γ	ratio of specific heat at constant pressure to that at constant volume
δ	boundary-layer thickness
δ^x	boundary-layer displacement thickness
ϵ	semiapex angle of delta wings
μ	dynamic viscosity
ρ	gas density
$\overline{\chi}$	viscous-interaction parameter
$\overline{\chi}_{c_r}$	viscous-interaction parameter with Reynolds number based on root chord of delta wing
ω	exponent in power law for viscosity

Subscripts:

e	recovery conditions
ins	insulated wall
0	supply conditions
turb	turbulent flow
w	wall

1	edge of boundary layer
Δ	delta wing
∞	free stream

Superscript:

*	ratio of conditions taking variation in γ into account to conditions with constant γ

APPARATUS AND METHODS

Tunnel and Nozzles

The investigation was conducted in the Langley 11-inch hypersonic tunnel, which operates intermittently. Three different nozzles were used during the tests: 2 two-dimensional nozzles, each of which provided a Mach number of slightly less than 7, and a three-dimensional nozzle with which a Mach number close to 10 could be obtained. The first two-dimensional nozzle had contours machined from steel and was replaced after the test program had started by a nozzle having contours constructed of Invar. Invar was used for the contour plates of the second nozzle because thermal gradients in the nozzle blocks caused objectionable deflection of the first minimum of the steel nozzle. In addition, the Invar nozzle was designed so that pressure gradients normal to the horizontal plane of symmetry were minimized. The three-dimensional nozzle had a square test section and first minimum, though nowhere else was the cross section square. This design allows the installation of conventional schlieren windows and reduces the possibility of incurring the axisymmetric imperfections at the wall that might occur in a circular nozzle and which would tend to focus along the axis of the nozzle.

A description of the tunnel may be found in reference 14 and a description of the steel nozzle and a calibration at a stagnation pressure of 25 atmospheres (R per inch = 250,000) in reference 15. Additional calibration data for the steel nozzle and some calibration data for the Invar nozzle are contained in reference 16. Figure 1 presents some of the calibration data obtained in the three-dimensional nozzle.

Models and Supports

Of the wings investigated, two had square plan forms (fig. 2) and the rest were a family of delta wings with symmetrical double-wedge

sections, a thickness ratio of $2\frac{1}{2}$ percent, and semiapex angles varying from 30° to 8°. The surfaces were ground and the leading edges were from 0.001 to 0.002 inch thick. The designations of these wings and their dimensions and sting dimensions are shown in figure 3.

For the measurement of surface pressures the model shown in figure 4 was used. This model was also equipped with thermocouples for the determination of skin temperature. The leading-edge thickness of this model was close to 0.0005 inch.

Instrumentation

The drag of the wing models was measured with a two-component strain-gage balance. This balance is temperature compensated and its sensitivity to uneven heating has been reduced to tolerable limits by shielding and insulation. For a more complete description of this balance see reference 17, where it is designated as the "sensitive two-component force balance."

The base pressure for use with the sting corrections to the wing force measurements and the surface pressures for the model shown in figure 4 were measured by means of the aneroid-type six-cell recording unit described in reference 14. The stagnation pressure was measured with Bourdon gages with an accuracy of about one-half of 1 percent.

Surface-Film Flow Studies

Surface flow studies of the square-plan-form wings and wings 3, 4-B, and 4-C were made by photographing the patterns made by streaming graphite and fluorescing mineral oil under ultraviolet light during a run. The wings were coated with SAE 30 lubricating oil before the run and graphite was spotted along the leading edge. The cameras were equipped with suitable filters to photograph the fluorescing oil to best advantage.

Tunnel Conditions

For the force tests of the wings at a Mach number near 7 the tunnel was operated at a stagnation temperature near 1,130° R, and for the square-plan-form wings it was operated through a stagnation-pressure range from 7 to 39 atmospheres (with Reynolds number per inch in the range from 0.08×10^6 to 0.43×10^6). Calibrations of these nozzles show a slight effect of Reynolds number per inch in the test range.

For example, at Reynolds numbers per inch of 0.08, 0.14, 0.20, 0.26, and 0.40 ($\times 10^6$) the corresponding Mach numbers are 6.67, 6.77, 6.82, 6.86, and 6.90.

For the determination of pressure distributions in the three-dimensional nozzle the stagnation temperature was close to 1,600° R and the flat surface of the pressure model (fig. 4) was located parallel to the XY-plane of the nozzle at Z = 3/4 inch, with the leading edge at X = -2 inches (fig. 1). The stagnation pressure was varied through the limited range from 31 to 46 atmospheres (with Reynolds number per inch from 0.075×10^6 to 0.11×10^6 when the variation in γ is taken into account). The Mach number in this nozzle (fig. 1) is about 9.6 if caloric imperfections (variable γ) are taken into account (ref. 18).

PRECISION OF DATA

For the force data obtained in the Mach number 7 nozzles, random errors in coefficients arise mainly in reading and recording balance forces and stagnation pressures, whereas the source of systematic errors is mainly in the possibility of an incorrect assessment of Mach number and the effect of the sting pressure field on the wing. The possible error resulting from errors in Mach number determination is small in comparison with the possible random errors, being about one-half of 1 percent of the coefficient values at Reynolds numbers per inch greater than about 200,000 and rising to perhaps 0.8 of 1 percent below this value.

The maximum possible errors in drag coefficient (ΔC_D) due to random factors, including sting corrections, are as follows (Reynolds number is based on root chord for the wings with delta plan form):

Wing	Plan form	R	ΔC_D
5-percent-thick diamond sections	Square	0.3×10^6 .5 .9 1.4	0.00075 .00044 .00024 .00016
Wedge-slab-wedge sections	Square	.5 .5 .9 1.4 2.4	.00031 .00031 .00021 .00015 .00014

Wing	Plan form	R	ΔC_D
1	Delta	0.7×10^6 1.4 2.1	0.00051 .00035 .00027
2	Delta	.9 1.4 2.1	.00047 .00029 .00025
3	Delta	1.0 1.6 2.7	.00051 .00031 .00024
4	Delta	1.5 2.0 2.7	.00046 .00036 .00032
4-A, 4-B, 4-C	Delta	2.3 2.6 3.0 4.0 4.8 5.4	.00023 .00020 .00017 .00014 .00009 .00014

The pressures measured on the flat plate at $M = 9.6$ have a possible error of about 2 percent due to inherent instrument inaccuracies.

RESULTS AND DISCUSSION

Theoretical Considerations and Comparison With Previous Data

The considerable distortion of the flow field about plane surfaces or slender bodies in hypersonic flows due to boundary-layer displacement effects is now well known qualitatively. In addition, a considerable body of quantitative theoretical evaluations of this effect is now available. These solutions in general fall into two classes: the so-called "weak interaction" and "strong interaction" solutions. Expressed rather simply, the weak-interaction solution is one in which the self-induced pressure gradient is assumed not to affect the boundary-layer growth, whereas in the strong-interaction solution account is taken of the effect on the boundary-layer growth of the mutual interaction between the boundary layer and the boundary-layer-induced pressure gradients. The

parameter which basically determines the region in which interaction effects can be important was first given by Lees and Probstein (ref. 1). This parameter is commonly designated $\overline{\chi}$, where

$$\overline{\chi} = \frac{M_\infty{}^3\sqrt{C}}{\sqrt{R}}$$

As shown subsequently, the weak-interaction theory for the insulated case applies in the region of $\overline{\chi}$ from 0 to approximately 1, whereas strong-interaction theory applies in the region of $\overline{\chi} \gg 1$. A leading edge of infinitesimal thickness is postulated.

Insulated plate in weak-interaction regime.- Into the category of weak-interaction solutions fall the theories formulated by Lees and Probstein (ref. 1) and Bertram (ref. 2). In terms of the parameter $\overline{\chi}$ the pressure distribution and skin friction for the insulated flat plate are as follows for large values of M and small flow deflections.

The Lees-Probstein solution for pressure distribution, to the second order, is

$$\frac{p}{p_\infty} = 1 + 0.599\gamma(\gamma - 1)\overline{\chi} + 0.090\gamma(\gamma - 1)^2(\gamma + 1)\overline{\chi}^2 \qquad \left(N_{Pr} = 1\right) \qquad (1)$$

$$\frac{p}{p_\infty} = 1 + 0.566\gamma(\gamma - 1)\overline{\chi} + 0.077\gamma(\gamma - 1)^2(\gamma + 1)\overline{\chi}^2 \qquad \left(N_{Pr} = 0.725\right) \qquad (2)$$

If Bertram's expression for the shape of the boundary-layer displacement thickness is put into the power-series expansion for pressure (with the product $M_\infty \frac{d\delta^x}{dx}$ small), to correspond with the Lees-Probstein theory, the second-order result is

$$\frac{p}{p_\infty} = 1 + 0.638\gamma(\gamma - 1)\overline{\chi} + 0.102\gamma(\gamma - 1)^2(\gamma + 1)\overline{\chi}^2 \qquad \left(N_{Pr} = 1\right) \qquad (3)$$

The difference in coefficients between equations (1) and (3) arises from a slight difference in the boundary-layer thickness values used in the theories. First-order weak-interaction theory consists of unity plus the first term in $\overline{\chi}$ in equations (1) to (3).

A simple expression for the local skin-friction coefficient is obtained in reference 2 from flat-plate theory, for a linear velocity profile in the boundary layer with no heat transfer:

$$C_f = \frac{2\mu_0}{\rho_\infty u_\infty^2} \frac{u_1}{\delta} \tag{4}$$

An expression for δ can be obtained by taking the result from reference 2 to hypersonic approximation (after Von Kármán, ref. 19). If the variables in the resulting equation are evaluated at the local conditions at the edge of the boundary layer, the result is:

$$\delta = \frac{2.553 \frac{\gamma - 1}{2} M_1^2 \sqrt{C_1}\, x}{\sqrt{\rho_1 u_1 x/\mu_1}} \tag{5}$$

Substituting equation (5) into equation (4) and utilizing the perfect gas law and the adiabatic relations between pressure, density, and temperature gives for local skin-friction coefficient the expression

$$C_f \frac{\sqrt{R}}{\sqrt{C}} = 0.7834\sqrt{p/p_\infty} \tag{6}$$

or, for comparison with the flat-plate theory without pressure gradient,

$$\frac{C_f}{C_f} = \sqrt{p/p_\infty} \tag{7}$$

In a fashion similar to that in which equation (6) was obtained, equation (5) may be written in terms of undisturbed free-stream conditions, and the normalized boundary-layer thickness is

$$\frac{\delta\sqrt{R}}{x\sqrt{C}} = 2.553 \frac{\gamma - 1}{2} M_\infty^2 (p/p_\infty)^{-1/2} \tag{8}$$

As will be seen by comparison with the results of strong-interaction theory presented subsequently, equations (6) to (8) will also apply as an approximation through the strong-interaction regime.

Kuo's closed-form results in reference 8 apparently apply to the weak-interaction region of plates since, with $M \to \infty$, his equation for pressure distribution is almost identical to equation (1). Kuo's evaluation of local skin-friction coefficient is composed of two opposing terms. With $M \to \infty$ the result obtained is

$$\frac{C_f\sqrt{R}}{\sqrt{C}} = \sqrt{\frac{p}{p_\infty}}\left[0.664 - \frac{1.192(0.679 - 0.347\gamma)(\gamma - 1)\bar{X}}{-F\bar{X} + \sqrt{1 + (F\bar{X})^2}} + \ldots\right] \tag{9}$$

where

$$\frac{p}{p_\infty} = 1 + 0.596\gamma(\gamma - 1)\bar{X}\left[F\bar{X} + \sqrt{1 + (F\bar{X})^2}\right]$$

and

$$F \equiv 0.149(\gamma - 1)(\gamma + 1)$$

Although equation (9) indicates an initial increase in skin friction over the no-interaction case with increasing $\bar{X}$, the skin friction eventually reaches a peak and then decreases rapidly.

Insulated plate in strong-interaction regime.- The strong-interaction regime has been investigated by Lees (refs. 6 and 7), Bertram (ref. 2), and Li and Nagamatsu (ref. 4). This regime is characterized by a boundary-layer growth of the form

$$\frac{\delta\sqrt{R}}{x\sqrt{C}} \propto \frac{M_\infty^2}{\sqrt{\bar{X}}}$$

for large values of M and $\overline{\chi}$. (See, for example, p. 261 of ref. 6.) The classical flat-plate laminar-boundary-layer growth used in the weak-interaction solution to obtain the induced-pressure distribution is

$$\frac{\delta\sqrt{R}}{x\sqrt{C}} \propto M_\infty^2$$

where M is large.

The results of the strong-interaction solutions apply, in general, for values of the interaction parameter $\overline{\chi}$ much greater than 1. Two main approaches to the strong-interaction problem are available. One is Shen's assumption (ref. 3), later extended by Li and Nagamatsu (ref. 4), that the edge of the boundary layer is also the shock induced by the boundary layer, and the second is the approach by Lees (refs. 6 and 7) and Bertram (ref. 2) in which the edge of the boundary layer (or the displacement thickness) is taken as the boundary of a new body. The effect of these differences in concept are discussed by Lees in reference 6.

The results of the Li-Nagamatsu theory may be put into the following form (for an insulated flat plate), which is consistent with the hypersonic approximations used in the theory:

$$\frac{p}{p_\infty} = \gamma\sqrt{\frac{\gamma - 1}{\gamma + 1}}\,\overline{\chi} - \frac{\gamma - 1}{\gamma + 1}$$

$$\left.\begin{aligned}
\frac{C_f\sqrt{R}}{\sqrt{C}} &= 2.27\,\frac{(\gamma - 1)^{3/4}}{(\gamma + 1)^{1/4}}\,\overline{\chi}^{1/2} \\
\frac{C_f}{\overline{C_f}} &= 2.89\,\frac{(\gamma - 1)^{3/4}}{(\gamma + 1)^{1/4}}\,\overline{\chi}^{1/2} \\
\frac{C_F\sqrt{R}}{\sqrt{C}} &= 9.1\,\frac{(\gamma - 1)^{3/4}}{(\gamma + 1)^{1/4}}\,\overline{\chi}^{1/2} \\
\frac{C_F}{\overline{C_F}} &= 5.80\,\frac{(\gamma - 1)^{3/4}}{(\gamma + 1)^{1/4}}\,\overline{\chi}^{1/2}
\end{aligned}\right\} \left(\overline{\chi}^2 \geqq \frac{3.91}{(\gamma + 1)(\gamma - 1)}\right)$$

$$\frac{C_F}{\overline{C_F}} = 1 + \left(4.12 - 0.506\sqrt{\frac{\gamma + 1}{\gamma - 1}}\right)(\gamma - 1)\overline{X} \qquad \left(\overline{X}^2 \leq \frac{3.91}{(\gamma + 1)(\gamma - 1)}\right)$$

For the Lees strong-interaction theory applied to the insulated flat plate the following results are obtained:

$$\frac{p}{p_\infty} = 0.52\overline{X} + 0.92 \qquad \text{(First order; } \gamma = 7/5\text{; } N_{Pr} = 1\text{)}$$

$$\frac{p}{p_\infty} = 0.92\overline{X} \qquad \text{(Zeroeth order; } \gamma = 5/3\text{; } N_{Pr} = 1\text{)}$$

$$\left.\begin{aligned} \frac{C_f\sqrt{R}}{\sqrt{C}} &= 0.55\overline{X}^{1/2} \\ \frac{C_f}{\overline{C_f}} &= 0.83\overline{X}^{1/2} \\ \frac{C_F\sqrt{R}}{\sqrt{C}} &= 2.20\overline{X}^{1/2} \\ \frac{C_F}{\overline{C_F}} &= 1.66\overline{X}^{1/2} \end{aligned}\right\} \text{(Zeroeth order; } \gamma = 7/5\text{; } N_{Pr} = 1\text{)}$$

In Bertram's theory, effects approaching strong interaction can be taken into account by an iteration procedure described in reference 2. However, with this method there is no distinction between strong and weak interaction, since the iteration procedure gives a continuous variation between the two regimes. Pai and Shen (ref. 9) present a theory in which, by matching the solution to both the strong- and weak-interaction regimes, a result is obtained which is also applicable through both regimes.

Shown in figure 5 are the pressure distributions given by the various theories for an insulated plate with $\gamma = 7/5$, together with Kendall's experimental results (ref. 11) for a flat plate in thermal equilibrium in air (surface temperature essentially equal to recovery temperature).

From various considerations, including the Knudsen number and the distance of the first orifice from the leading edge (in terms of leading-edge thickness), the effect of leading-edge blunting on these pressures is believed to be small. Leading-edge-thickness effects are discussed further in appendix A. The curve for Bertram's theory was calculated for $M = 9.6$ by the iteration scheme described in reference 2 by use of isentropic compressions and continuous variations in dM/dx. Though this Mach number is considerably higher than 5.8, the curve should be applicable to the data for lower Mach numbers since this curve agreed with the results from the iteration process for $M = 6.86$ presented in reference 10 in the region of $\overline{X}$ where they overlapped. The process of using the result of a first iteration to start a second iteration, and so on, does not appear to be convergent. However, by averaging between assumed and resulting pressure distributions for successive iterations the results can be made convergent in the range of $\overline{X}$ below about 10. The second-order weak-interaction theory for air appears to agree well with experiment in the range of $\overline{X}$ from about 0 to 2. The Lees strong-interaction, the Pai-Shen, and the Bertram theory agree well with experiment over the entire range in which experimental data are available (up to $\overline{X} \approx 3$). The Li-Nagamatsu theory would not be expected to apply at the low values of $\overline{X}$. The curve shown in figure 5 for the Li-Nagamatsu theory does not agree with that given in figure 17 of reference 12. However, it can be shown that the curve given in reference 12 is incorrect and does not apply even when $C = 1$.

The theoretical local and average skin-friction coefficients for the insulated plate are shown in figure 6 divided by the value given by flat-plate theory without interaction effects. Also shown are the experimental average skin-friction coefficients over the limited range of $\overline{X}$ obtained by Kendall (ref. 11), using the Eimer-Nagamatsu results as the interaction-free denominator (ref. 20). There is essential agreement between the Bertram theory with pressure gradient and the Lees strong-interaction theory; however, the Li-Nagamatsu theory predicts skin frictions which are considerably higher than those of either of the foregoing theories. The experimental results apparently favor the Bertram theory, which at the largest value of $\overline{X}$ of the experimental data predicts a skin friction about 25 percent below that given by the Li-Nagamatsu theory. Such correlation between theory and experiment, however, cannot be considered to be conclusive in this case since some question arises as to the accuracy of the data. If the local skin-friction coefficients are multiplied by the factor 2, which is assumed to give the average skin-friction coefficient, $C_F\sqrt{R} \approx 1.07$ from the Eimer-Nagamatsu experiments whereas theoretically, for the no-interaction case, $C_F\sqrt{R}$ is approximately 1.35 (ref. 21). The cause for the discrepancy is unexplained. In addition, although the investigations of references 11 and 20 were conducted in the same wind tunnel, the methods

of evaluating skin friction were different. This difference is expected to be an additional source of error, though less important than the discrepancy involved above.

Noninsulated plate.- The case of the noninsulated plate has not been investigated as extensively as that of the insulated plate. Qualitatively, it is easily seen that heating the plate above the recovery temperature will increase the boundary-layer-interaction effects through thickening of the boundary layer, whereas the reverse will be true if the plate is cooled below recovery temperature because the boundary layer will be thinned.

In treatments of the interaction problem when heat transfer is present, the wall temperature is generally considered constant. For the weak-interaction case, Lees and Probstein give a solution (ref. 1) including heat transfer from which the induced-pressure effect may be obtained in closed form. For the strong-interaction region there are several recent analyses of the effect of heat transfer when the wall temperature is invariant. Lees (ref. 6) gives zeroeth-order results when the heat transfer is very large (wall temperature near 0°) and Li and Nagamatsu (ref. 22) give zeroeth-order results for a wide range of wall temperatures and γ values of 1.4 and 1.67. These results agree in regions where the two may be compared, even though reference 22 makes the considerably simplifying assumption that $C = 1$ in the linear formula for viscosity. However, the values given in reference 22 for the coefficient used to evaluate the Stanton number are too high by a factor of 2. The results of Pai and Shen (ref. 9), as mentioned previously, apply through the weak- and strong-interaction regimes.

Experiment

Pressure measurements in air at $M_\infty = 9.6$.- The pressure distributions at a Mach number of 9.6 were obtained on a flat plate in the three-dimensional nozzle with heat transfer from the boundary layer to the plate surface. The heat transfer is a result of the short duration of the test run combined with the initially low flat-plate temperature (about room temperature) and the high stagnation temperature (about 1,600° R). This pressure distribution is shown in figure 7, together with the values given by theory for an insulated flat plate (from fig. 5). The measured pressures are considerably overestimated by insulated-plate theory. The pressures presented are those for 85 seconds after the start of a run and the temperatures for the same time are shown in figure 8.

As a first approximation it was decided to calculate the effect of the temperature gradient and heat-transfer conditions on boundary-layer thickness independently of the pressure-gradient effects. To this end

the Chapman-Rubesin theory (ref. 23) was utilized with a free-stream Mach number of 9.6. The second-degree equation shown at the top of figure 8 was taken to represent the temperature distribution (the recovery temperature was arbitrarily selected to be about 0.85 of the stagnation temperature). Computations were then carried out to determine the displacement thickness at the 15-, 30-, 60-, and 100-percent-chord points. The results of these calculations are shown in the two lower plots of figure 8. The corrections to the insulated-plate results were obtained simply by modifying the slope of the boundary-layer displacement thickness calculated for the insulated flat plate, as follows:

$$\frac{d\delta^x}{dx} = \frac{\delta^x}{\delta^x_{ins}} \frac{d\delta^x_{ins}}{dx} + \frac{\delta^x_{ins}}{L} \frac{d\left(\frac{\delta^x}{\delta^x_{ins}}\right)}{d\left(\frac{x}{L}\right)}$$

The ratios δ^x/δ^x_{ins} and $d\left(\delta^x/\delta^x_{ins}\right)/d(x/L)$ were obtained from the Chapman-Rubesin theory, and the values for $d\delta^x_{ins}/dx$ and δ^x_{ins}/L were computed according to the theory with pressure gradient of reference 2.

This correction to the slope of the boundary-layer displacement thickness on an insulated flat plate resulted in the pressure distribution shown in figure 7 as the dashed line. The agreement with the experimental results is surprisingly good. For comparison with the computations that include heat transfer and temperature gradient, the effect of a constant ratio of wall to stream temperature was computed from the Chapman-Rubesin theory by using an approximately average temperature ratio from the experiments ($T_w/T_\infty \approx 9$). The resulting value of δ^x/δ^x_{ins} is shown in figure 8; it is not an average value of the change in the displacement thickness due to heat transfer but, as expected, is too low a value and thus would underestimate the pressures on the average. The heat transfer itself, however, has much more effect on the pressures than the temperature-gradient term.

In figure 7 the data at the lowest values of $1/\sqrt{R_x}$ (highest Reynolds numbers) approach the base line of zero pressure difference at a faster rate than is predicted by theory. This is apparently the same phenomenon as was observed in the Princeton helium tunnel on similar models (figs. 11, 12, and 14 of ref. 12) and eliminated in the final plots of the helium-tunnel results (figs. 15 to 18 of ref. 12). There can apparently be an under or over pressure, depending on the mounting and the shape of the back and side of the model, and figure 11 of reference 12 indicates that there is a strong Reynolds number effect. These side and base effects appear to be propagated for large distances both upstream and laterally.

In the present tests pressure orifices were located laterally at the middle and last station on the plate (see fig. 4). The resulting pressure differences are shown in figure 9 as a function of the local lateral distance to the orifice nondimensionalized with respect to local lateral distance to the model edge. There is considerable scatter in the data, much of which is attributable to the low pressure being measured (about 1 mm of mercury) but the general trend of a decrease in pressure as the model edge is approached is evident. The decrease in pressure from the center to the outermost orifice is considerably larger for the rearmost set of orifices.

All the data from orifices on or near the model center line have been included in figure 7; thus some of the data are from the orifices between 2 and 4 inches from the leading edge ($\overline{X}$ less than about 2.5). This is the region in which the side effects discussed previously are important, and therefore the results from this region may be somewhat in error.

Figure 10 presents the experimental results originally given in figure 7; however, instead of modifying the theory to account for heat transfer and temperature gradient, the theoretical increment in pressure attributable to heat transfer has been added to the data for $M = 9.6$. The good agreement of these data with the Lees, Pai-Shen, and Bertram theories is notable, as is the correlation with Kendall's data for $M = 5.8$.

Real-gas effects.- In the evaluation of Mach number and the other associated flow properties of a gas it is important to determine the effects associated with actual gas flows. In most supersonic wind tunnels it is sufficient to use the perfect gas law and assume that γ is constant. At the high supply pressures and stagnation temperatures at which hypersonic tunnels are operated these assumptions, however, can be invalidated.

An analysis of the effect of variable specific heats on the gas properties has been given by Eggers (ref. 24). The equations given in reference 24 have been combined with the Sutherland formula to determine the effect of caloric imperfections on parameters basic to the boundary-layer analysis. The additional assumption has been made that the static temperature is much less than the stagnation temperature. For the range of stagnation temperature shown in figure 11 (1,000° R to 5,000° R), this assumption corresponds to the restriction that the static temperature be less than approximately 500° R. The equations which describe the curves in figure 11 are given in appendix B. For the present tests the stagnation temperature was close to 1,600° R. For a pressure ratio of 30×10^{-6} (see fig. 1) the Mach number was found to be close to 9.6.

The Reynolds numbers computed for the conditions at this Mach number were corrected according to figure 11 with $\beta/T_{P,\infty} = 2.1$. In the present tests the effects of variable gamma were not large. The question then arises as to the magnitude of imperfect-gas effects.

With the assumption that the Berthelot equation of state in virial form is applicable, equations describing imperfect-gas effects have been derived in appendix B. In equation (B11) the following values were then used: $T_c = 238.5^\circ$ R, $p_c = 547$ lb/sq in. abs (the values for air); $T_0 = 1,600^\circ$ R, $p_0 = 647$ lb/sq in. abs, $p_\infty = 0.0194$ lb/sq in. abs (experimental values); $T_\infty = 82^\circ$ R, $\gamma = 7/5$ (assumed values). The resulting static-temperature ratio given by equation (B11) was found to be only one-half of 1 percent greater than would be given by the ideal-gas equation ($p = \rho RT$, $\gamma = 7/5$). This increase is small compared with the 3.3-percent increase in this same temperature parameter indicated by equation (B3) for the effect of variable γ. Therefore imperfect-gas effects were ignored in analyzing the data.

Drag measurements at $M_\infty = 6.8$.- The results of total-drag measurements in coefficient form for two square wings and a series of delta wings are presented in figure 12. Leading-edge thickness was determined for each wing from an examination of the leading edge through a calibrated microscope. The pressure acting on the leading edge was assumed to be given by the average between $C_{p,max}$ and the average pressure coefficient over the front half of a cylinder. The drag coefficient given by the average pressure coefficient $\left(C_{p,t} = (5/6)C_{p,max}\right)$ was subtracted from the total drag coefficient for presentation in figure 12. For the delta wings $C_{p,max}$ was assumed to vary as the square of the sine of the semiapex angle. Following are the estimated leading-edge drag coefficients $C_{D,t}$ in terms of projected wing area:

Plan form	Wing	t, in.	$C_{D,t}$
Square	Diamond sections	0.001	0.00038
	Wedge-slab-wedge sections	.002	.00056
Delta	1	0.001	0.00018
	2	.001	.00006
	3	.001	.00002
	4	.002	.00002
	4-A, 4-B, 4-C	.0008	.00000

For the purpose at hand, that of determining skin friction by using wings with a very low pressure drag, the square wing with 5-percent-thick diamond sections had an undesirably high pressure drag; however, this wing was the only one for which local pressures were available (the investigation reported in ref. 17). In the final analysis the square wing with wedge-slab-wedge sections was hampered by a drag due to leading-edge thickness which was about double the value that would be obtained for inviscid pressure drag if the leading-edge thickness were nonexistent ($C_{D,p} = 0.00030$ compared with $C_{D,t}$ values given in preceding table).

For the square wings (at the top of fig. 12) the drag obtained by adding the skin friction, with the effect of the self-induced pressure gradient included, to the theoretical inviscid pressure drag is generally closer to the experimentally determined drag than if the classical flat-plate skin friction is used. The total experimental drag is 10 to 30 percent higher than is given by a combination of classical laminar skin friction and the inviscid pressure-drag coefficient. There are a great many unknowns still involved in the effects of viscosity on the drag of the rear surface, including tip, trailing-edge, and displacement effects. According to pressure measurements on the center line of the square wing with diamond sections at zero angle of attack (fig. 4(a) of ref. 17) the displacement effect on the front surfaces causes an incremental increase in pressure drag of 11 percent; however, this increase is partially compensated by an incremental decrease of about 40 percent in pressure drag of the rear surfaces due to displacement and trailing-edge shock effects. The result is an indicated 28-percent decrease in pressure drag from the theoretical prediction.

An indication of tip effects on the square wing with the diamond section, at least at one Reynolds number, can be seen in figure 13(a) from an oil-flow study of the wing surface at a Reynolds number of 1.2×10^6. The oil flow on this wing was examined by means of both still and motion pictures. The significant extent of tip effects appears to be confined to the rear surface and consists of a roughly triangular region indicative of either a shock or separated flow. The dark areas near the leading edge of the wings shown in figures 13 and 14 are caused by the high laminar shear near the leading edge, which quickly wipes the oil from this region.

Figure 13(b) shows the oil flow on the upper surface of the square wing with wedge-slab-wedge sections, and figure 13(c) shows the flat lower surface of this wing. The rear surface of this wing is small, and although the flow phenomenon is similar to that on the diamond-section wing, the separation is confined to a correspondingly smaller portion of the trailing wing tip. In addition to this separation (or shock) a three-dimensional edge flow can be seen. On the lower surface the region of three-dimensional edge flow is delineated by the high shear

which scrubbed the oil from the surface near the side edges. On this surface the angle that this scrubbed area makes with the wing edge is about 2°. On the upper surface a disturbance can be seen to extend farther inboard than the area actually scrubbed clean. The total area affected seems to make an angle with the wing side edge of about 3.5°. For both wings the area significantly influenced by the tip flow is small; however, the effects on the total drag may be significant because of the indicated increase in surface shear in the tip region.

At the bottom of figure 12 are the data for the family of $2\frac{1}{2}$-percent-thick delta wings with semiapex angles varying from 30° to 8° and symmetrical double-wedge sections. The theoretical skin-friction-coefficient curves for these wings differ from those presented for the square wings only in their adaption to the delta plan form, as shown in appendix C. The wave drag shown in the figure for these delta wings is that given by two-dimensional shock-expansion theory for the streamwise wing section (assuming the compensating pressure effects on the front and rear wing surfaces discussed previously for the square wings). This wave drag has been added to the skin friction with displacement effect to obtain the curve coded with short dashes in this figure. For the range of semiapex angles shown there is good correlation of the experimental data over the entire range of Reynolds number (based on root chord). At the lower Reynolds numbers $\left(R_{c_r} < 1.3 \times 10^6\right)$ the theoretical skin friction with displacement effect plus the two-dimensional wave drag gives an excellent representation of the data (wings 1, 2, and 3) and is 20 to 30 percent higher than the drag obtained by a combination of the classical skin friction and inviscid pressure drag. Above this Reynolds number, however, there is a progressive departure of the experimental data from the laminar theory. This result for $R_{c_r} > 1.3 \times 10^6$ is taken to be indicative of transition of the boundary layer. The data for the square wings in figure 12 indicate a similar trend at the higher Reynolds numbers. It should be noted that the value of 1.3×10^6 for the Reynolds number based on root chord corresponds to a different unit Reynolds number for each wing. For delta wings 1, 2, and 3 this Reynolds number corresponds to Reynolds numbers per inch of 0.30×10^6, 0.24×10^6, and 0.19×10^6, respectively.

Oil-flow studies of the delta wing (fig. 14) have shown that the only deviations from disturbance-free flow on the surface are manifested in the region of the sting. The disturbance is indicated by the dark, approximately triangular area emanating from the point of the sting, where the oil has been wiped from the surface. Wing 1 ($\epsilon = 30^{\circ}$) shows very little sting interference. (See fig. 14(a).) This wing and wings 2 and 3 had a very narrow sting (0.091 to 0.092 inch). In contrast, the oil-flow photographs of wings 4-C and 4-B (figs. 14(b)

and 14(c)) show well-defined regions of sting interference. The wings of the number 4 series had thicker stings (see fig. 3) than wings 1, 2, and 3. The results for wings 4-A, 4-B, and 4-C in figure 12 indicate that the pressure field from the stings has only a small direct influence on the drag, even though the length of sting covering the root chord was varied from 0.43 of the root chord down to 0.19 of the root chord. In view of the low pressure drag of these airfoils, this result is not surprising. For wing 4-C, which was tested in two nozzles with very nearly the same test-section Mach number, there was no really significant difference between the data obtained in the two nozzles. The data from the two nozzles is, in general, within the band given by the possible error. (See section entitled "Precision of Data.")

Computations were made to determine the effect that the sting would have if it were assumed to cause transition of the boundary layer. To simplify matters, a triangular flat plate with zero inclination to the stream was assumed, with transition parallel to the leading edge at various fractions of the root chord, a. For comparison with the hypothetical wing, the experimental results from figure 12 for the delta wings are shown in figure 15 with an assumed constant value of pressure drag coefficient (0.00037) subtracted. The curve for transition fixed at about 0.7 of the root chord fits the data over a considerable range of Reynolds numbers. Because of the relatively small increase in measured drag over the drag predicted when classical flat-plate laminar-boundary-layer theory is used, attributing the increase to displacement effects must be considered inconclusive. However, from figure 12 it appears that this increase in drag, for the lower Reynolds numbers at least (considering the thinness of the mounting sting and the thickness of the boundary layer), is caused by displacement effect. At Reynolds numbers greater than about 1.3×10^6 the drag is higher than can be accounted for by any cause but transition.

CONCLUDING REMARKS

Measurements are presented for boundary-layer-induced pressure gradients on a flat plate in air at a Mach number of 9.6 and for the drag of thin wings at a Mach number of about 6.8 and zero angle of attack. The pressure measurements at a Mach number of 9.6 were made in the presence of substantial heat transfer from the boundary layer to the plate surface. The measured pressure distribution on the surface of the plate was predicted with good accuracy by a modification to insulated-plate displacement theory which allows for the effect of the heat transfer and temperature gradient along the surface on the boundary-layer displacement thickness.

The total drag of thin square and delta wings was measured at a nominal Mach number of 6.8 over a reasonably wide range of Reynolds numbers. This total drag was found to be greater, by as much as 30 percent, than can be explained by adding a classical value of laminar skin friction to the estimated pressure drag. The difference is, in general, explained by the effect of boundary-layer-induced pressures on skin friction. At Reynolds numbers above about 1.3×10^6 an additional increase in skin friction was measured, which is attributed to transition of the boundary layer.

Langley Aeronautical Laboratory,
National Advisory Committee for Aeronautics,
Langley Field, Va., November 15, 1957.

APPENDIX A

LEADING-EDGE-THICKNESS EFFECTS

The question of the contribution of leading-edge effects to the measured pressures arises. Two obvious factors which have to be evaluated are the (characteristic) boundary-layer thickness in comparison with the leading-edge thickness and the mean free path of the gas in comparison with the leading-edge thickness.

The assumption is made that this boundary-layer thickness for the laminar case may be represented by the simple equation

$$\delta = K \frac{x}{\sqrt{R_x}} \tag{A1}$$

The Reynolds number with radius of curvature of the edge of the boundary layer as the characteristic length is then

$$R_r = \frac{4}{K}\left(R_x + \frac{K^2}{4}\right)^{3/2}$$

At the leading edge

$$R_{t,\delta} \equiv 2R_r = K^2$$

With a linear velocity profile and $M \to \infty$ on an insulated plate,

$$K = 2.553 \frac{\gamma - 1}{2} M_\infty^2 \sqrt{C}$$

where C is the coefficient in the viscosity relation

$$\frac{\mu_w}{\mu_\infty} = C \frac{T_w}{T_\infty}$$

or, to eliminate the viscosity ratio as such, the power law or Sutherland's law for viscosity may be used to give, with hypersonic approximation for the insulated plate and $N_{Pr} = 1$,

$$C = \left(\frac{\gamma - 1}{2}\right)^{\omega-1} M_\infty^{2(\omega-1)} = \left(\frac{\gamma - 1}{2}\right)^{1/2} \frac{M_\infty\left(1 + \frac{\beta}{T_\infty}\right)}{\frac{\gamma - 1}{2} M_\infty^2 + \frac{\beta}{T_\infty}}$$

where ω is the exponent in the power law for viscosity. Thus

$$K = 2.553\left(\frac{\gamma - 1}{2}\right)^{\frac{1+\omega}{2}} M_\infty^{1+\omega}$$

and

$$R_{t,\delta} = 6.518\left(\frac{\gamma - 1}{2}\right)^{1+\omega} M_\infty^{2(1+\omega)}$$

or

$$\frac{R_{t,\delta}}{R_t} = 6.518\left(\frac{\gamma - 1}{2}\right)^{1+\omega} \frac{M_\infty^{2(1+\omega)}}{R_t} \tag{A2}$$

The question of whether the flowing gas will "see" the leading edge fully, imperfectly, or not at all should be answered by the Knudsen number N_{Kn}, which is the ratio of the molecular mean free path to the characteristic length (in this case the leading-edge thickness):

$$N_{Kn} = \frac{R_L}{R_t} = \frac{1.256\sqrt{\gamma}\, M}{R_t}$$

where R_L is the Reynolds number with mean free path as the characteristic length and the slip-flow regime is taken as

$$\frac{1}{100} < N_{Kn} < 2$$

The fact that equation (A1) does not represent the boundary-layer growth near the leading edge is ignored because for present purposes all that is desired is an index of the boundary-layer-induced effects on the plate. Whether equation (A2) can give some idea of the relative magnitude of the boundary-layer-induced effects and leading-edge-thickness effects can perhaps be decided by recourse to the available reports of experimental work. The work of Bertram (ref. 10), Kendall (ref. 11), and Hammitt and Bogdonoff (ref. 13) is useful in this regard. The range of these tests is shown in the table below:

Author	Ref.	M_∞	$R_{t,\delta}$	R_t	$\frac{R_{t,\delta}}{R_t}$	$N_{Kn} = \frac{R_L}{R_t}$
Bertram	10	6.9	625	370 to 1,960	1.7 to 0.32	0.028 to 0.0052
Kendall	11	5.8	260	14 to 47	19 to 5.5	0.62 to 0.18
Hammitt and Bogdonoff	13	11.8 11.4	3,660 3,300	940 to 42,500	3.9 to 0.07	0.02 to 0.0004
Present tests	--	9.6	900	38 to 56	24 to 16	0.38 to 0.26

For the experiments of Kendall (ref. 11), the results of which are probably the best yet obtained in air, the combination of the large values of the ratio $R_{t,\delta}/R_t$ shown in the table and a large Knudsen number which is apparently well into the slip-flow regime indicates that the leading-edge-thickness effects should be small compared with the boundary-layer effects. These data did not show an effect of R_t on surface pressure in the range of R_t of the investigation. In contrast, the range of $R_{t,\delta}/R_t$ for Bertram's tests in air (ref. 10) indicates that the leading-edge-thickness effects should range from small to a magnitude approximately equal to that of the boundary-layer effects and the leading-edge thickness is in general in the continuum regime. The results of pressure measurements in reference 10 show leading-edge-thickness effects over the test range that are of the order expected from consideration of equation (A2) of the present paper.

Hammitt and Bogdonoff's test range in the Princeton helium tunnel (ref. 13) is indicated (in the preceding table) to extend from a region in which the boundary-layer-induced effects are about 3 times the leading-edge-thickness effects to a region where the boundary-layer-induced effects are small compared with the leading-edge-thickness effects; however, over the entire range the leading edge is in continuum flow. The pressure data of reference 13 bear out this prediction in that, for values

of the index $R_{t,\delta}/R_t$ less than approximately 0.2, the pressure data correlate well when plotted against the inviscid parameter x/t. Significant deviation from correlation is first noted at $R_{t,\delta}/R_t = 0.55$, and at $R_{t,\delta}/R_t = 0.9$ the measured pressure rises are about twice the values given by the essentially inviscid pressure data at the same value of x/t. The deviation from correlation is even greater at $R_{t,\delta}/R_t = 3.9$.

The data of the present tests are in the same region of slip flow for the leading-edge thickness as Kendall's data, and by equation (A2) the viscous effects are still larger in comparison with leading-edge-thickness effects. The present results have values of the ratio $R_{t,\delta}/R_t$ which are as large as the largest value encountered in the Princeton tests (ref. 13) and the leading edge is farther into the slip-flow region. Leading-edge effects would not be expected in the present experiments and none could be detected over the limited range of R_t.

APPENDIX B

EFFECT OF VARIABLE γ AND GASEOUS IMPERFECTIONS

The problem of evaluating the effect of caloric imperfections (variable specific heats) may be greatly simplified by considering the stagnation temperature to be much larger than the static temperature. In this case the analysis of reference 24 can be used in the following simplified form (perfect gas law).

For the Mach number,

$$\frac{\gamma - 1}{2} M_\infty^2 = \frac{T_0}{T_\infty}\left[1 + \frac{\gamma - 1}{\gamma}\frac{\theta}{T_0}\left(e^{\theta/T_0} - 1\right)^{-1}\right] - 1 \tag{B1}$$

where θ is the molecular vibrational constant.

With the values of p_∞ and p_0 obtained experimentally, the required temperature ratio is given by

$$\frac{T_\infty}{T_0} = \left[\frac{p_\infty}{p_0}\frac{\exp\left(\frac{\theta}{T_0}\frac{e^{\theta/T_0}}{e^{\theta/T_0} - 1}\right)}{e^{\theta/T_0} - 1}\right]^{\frac{\gamma-1}{\gamma}} \tag{B2}$$

If an asterisk is used to signify the ratio of the indicated parameter to the value of that parameter when the ratio of specific heats γ is taken as constant, then the following relations are obtained:

$$M^* \equiv 1$$

$$\left(\frac{T_\infty}{T_0}\right)^* = 1 + \frac{\gamma - 1}{\gamma}\frac{\theta}{T_0}\left(e^{\theta/T_0} - 1\right)^{-1} \tag{B3}$$

$$\left(\frac{p_\infty}{p_0}\right)^* = \left[\left(\frac{T_\infty}{T_0}\right)^*\right]^{\frac{\gamma}{\gamma-1}}\left(e^{\theta/T_0} - 1\right)\exp\left(-\frac{\theta}{T_0}\frac{e^{\theta/T_0}}{e^{\theta/T_0} - 1}\right) \tag{B4}$$

$$\left(\frac{\mu_\infty}{\mu_0}\right)^* = \left[\left(\frac{T_\infty}{T_0}\right)^*\right]^{3/2} \frac{1 + \left(\beta/T_{P,\infty}\right)}{\left(T_\infty/T_0\right)^* + \left(\beta/T_{P,\infty}\right)} \tag{B5}$$

$$R^* = \frac{\left(p_\infty/p_0\right)^*}{\left(\mu_\infty/\mu_0\right)^* \sqrt{\left(T_\infty/T_0\right)^*}} \tag{B6}$$

where β is the Sutherland constant and $T_{P,\infty}$ the static temperature evaluated for constant γ. The much used coefficient in the linear formula for viscosity becomes

$$C^* = \frac{\left(T_\infty/T_0\right)^*}{\left(\mu_\infty/\mu_0\right)^*} \tag{B7}$$

Equation (B7) is valid for all wall temperatures. The hypersonic interaction parameter $\bar{\chi}$ then becomes (for all wall temperatures)

$$\bar{\chi}^* = \sqrt{\frac{C^*}{R^*}} = \sqrt{\frac{\left[\left(T_\infty/T_0\right)^*\right]^{3/2}}{\left(p_\infty/p_0\right)^*}} \tag{B8}$$

By using 5,500° R for the value of the molecular vibrational constant θ and $\gamma = 7/5$, figure 11 was constructed from these equations. For the range of stagnation temperature shown (1,000° to 5,000° R), the static temperature must be less than about 500° R for excellent accuracy. The Mach numbers at the top of the figure indicate the approximate limitations at integral temperatures imposed by the assumption of low static temperature.

Now, if the ratio of specific heats γ is assumed to be a constant, a simple solution for imperfect-gas effects may be obtained. The equation of state for a gas at moderate pressures, when only the first two terms in a series representation are used, is

$$p = \rho(\bar{R}T + Bp)$$

where B is known as the second virial coefficient in the expansion and $\bar{R}$ is the gas constant. The differential equation for an adiabatic process, to the same approximation, is (p. 180 of ref. 25)

$$\frac{\gamma - 1}{\gamma}\frac{dp}{p} = \frac{dT}{T}\left(1 + \frac{p}{\bar{R}}\frac{dB}{dT}\right) \tag{B9}$$

If Berthelot's value for B (p. 119 of ref. 25) is used:

$$B = \frac{9}{128}\frac{\bar{R}T_c}{p_c}\left(1 - \frac{6T_c^2}{T^2}\right)$$

and γ is taken as constant, the exact solution of equation (B9) is

$$\frac{T_\infty}{T_0} = \left(\frac{p_\infty}{p_0}\right)^{\frac{\gamma-1}{\gamma}}\left[1 + \frac{27}{32}\frac{\left(\frac{T_c}{T_0}\right)^3\frac{p_0}{p_c} - \left(\frac{T_c}{T_\infty}\right)^3\frac{p_\infty}{p_c}}{\frac{3 - 2\gamma}{\gamma} + \frac{27}{32}\left(\frac{T_c}{T_\infty}\right)^3\frac{p_\infty}{p_c}}\right]^{\frac{\gamma-1}{\gamma}} \tag{B10}$$

or, since the deviations from the perfect gas are assumed to be small,

$$\frac{T_\infty}{T_0} = \left(\frac{p_\infty}{p_0}\right)^{\frac{\gamma-1}{\gamma}}\left[1 + \frac{27}{32}\frac{\gamma - 1}{\gamma}\frac{\left(\frac{T_c}{T_0}\right)^3\frac{p_0}{p_c} - \left(\frac{T_c}{T_\infty}\right)^3\frac{p_\infty}{p_c}}{\frac{3 - 2\gamma}{\gamma} + \frac{27}{32}\left(\frac{T_c}{T_\infty}\right)^3\frac{p_\infty}{p_c}}\right] \tag{B11}$$

APPENDIX C

SKIN FRICTION OF A FLAT-PLATE WING WITH DELTA PLAN FORM INCLUDING BOUNDARY-LAYER DISPLACEMENT EFFECT

In this appendix a solution is derived for the skin friction with boundary-layer displacement effect on the flat-plate wing shown in the following sketch:

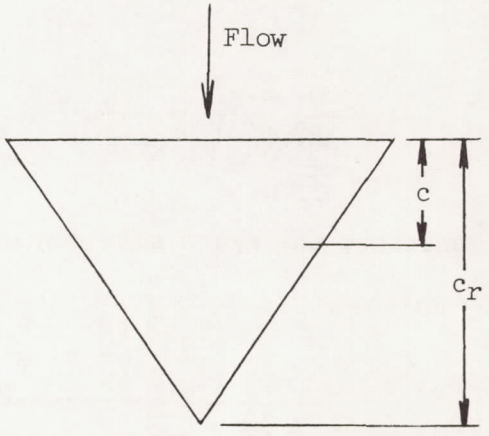

The assumption is made that each filament in the stream and boundary layer over the wing remains unaffected by adjacent filaments, and thus that any section of this wing may be treated as a section of an unswept flat plate with the local chord the same. The average skin-friction coefficient for the delta-plan-form flat plate is, then,

$$C_{F,\Delta} = \frac{2}{c_r^2} \int_0^{c_r} C_F c \, dc$$

or, in terms of the hypersonic interaction parameter,

$$C_{F,\Delta} = 4\bar{x}_{c_r}^4 \int_{\bar{x}_{c_r}}^{\infty} C_F \frac{d\bar{x}}{\bar{x}^5} \tag{C1}$$

where $\bar{x} = M_\infty^3 \sqrt{C} / \sqrt{R_c}$ and $\bar{x}_{c_r} = M_\infty^3 \sqrt{C} / \sqrt{R_{c_r}}$, where, in turn, R_c

and R_{c_r} are the Reynolds numbers based on local chord and root chord, respectively, and C is the coefficient in the linear formula for viscosity.

If $\overline{C_F}$ is the average skin-friction coefficient obtained from classical flat-plate boundary-layer theory (in effect, the Blasius solution), in order to simplify the solution the following relations are assumed:

$$\frac{C_F}{\overline{C_F}} = b'\bar{x}^{1/2} \qquad \left(\bar{x} \geq \bar{x}_o\right) \qquad (C2)$$

$$\frac{C_F}{\overline{C_F}} = 1 + a'\bar{x} \qquad \left(\bar{x} \leq \bar{x}_o\right) \qquad (C3)$$

The value $\bar{x}_o$ is the matching point between equations (C2) and (C3) where it can be shown that

$$\bar{x}_o = \frac{1}{a'} = \frac{4}{(b')^2} \qquad (C4)$$

When $\bar{x} \geq \bar{x}_o$, equation (C2) can be substituted into equation (C1) to obtain

$$C_{F,\Delta} = 4\bar{x}_{c_r}^{4} b' \int_{\bar{x}_{c_r}}^{\infty} \overline{C_F} \frac{d\bar{x}}{\bar{x}^{9/2}} \qquad (C5)$$

From appendix D (eq. (D18)):

$$\overline{C_{F,\Delta}} = \frac{4}{3} \frac{A}{\sqrt{R_{c_r}}} \qquad (C6)$$

where

$$\overline{C_F} = \frac{A}{\sqrt{R_c}}$$

Then equation (C5) is

$$\frac{C_{F,\Delta}}{\overline{C_{F,\Delta}}} = 3\bar{x}_{c_r}{}^{3} b' \int_{\bar{x}_{c_r}}^{\infty} \frac{d\bar{x}}{\bar{x}^{7/2}} \tag{C7}$$

which, upon integration, becomes

$$\frac{C_{F,\Delta}}{\overline{C_{F,\Delta}}} = \frac{6}{5} b' \bar{x}_{c_r}{}^{1/2} \qquad \left(\bar{x}_{c_r} \geq \bar{x}_o = \frac{1}{a'}\right) \tag{C8}$$

When $\bar{x} \leq \bar{x}_o$, equations (C2) and (C3) can be substituted into equation (C1) to obtain

$$C_{F,\Delta} = 4\bar{x}_{c_r}{}^{4} \left(b' \int_{\bar{x}_o}^{\infty} \overline{C_F}\, \bar{x}^{-9/2} d\bar{x} + \int_{\bar{x}_{c_r}}^{\bar{x}_o} \overline{C_F}\, \bar{x}^{-5} d\bar{x} + a' \int_{\bar{x}_{c_r}}^{\bar{x}_o} \overline{C_F}\, \bar{x}^{-4} d\bar{x} \right)$$

which is combined with equation (C6) and the result is integrated to give

$$\frac{C_{F,\Delta}}{\overline{C_{F,\Delta}}} = 1 + \frac{3}{2} a' \bar{x}_{c_r} + \bar{x}_{c_r}{}^{3} \left(\frac{6}{5} \frac{b'}{\bar{x}_o{}^{5/2}} - \frac{3}{2} \frac{a'}{\bar{x}_o{}^{2}} - \frac{1}{\bar{x}_o{}^{3}} \right) \qquad \left(\bar{x}_{c_r} \leq \bar{x}_o\right) \tag{C9}$$

or, by substituting equation (C4) into equation (C9),

$$\frac{C_{F,\Delta}}{\overline{C_{F,\Delta}}} = 1 + \frac{3}{2} a' \bar{x}_{c_r} - \frac{\left(a' \bar{x}_{c_r}\right)^{3}}{10} \qquad \left(a' \bar{x}_{c_r} \leq 1\right) \tag{C10}$$

Equation (C8) may also be written in terms of a' as

$$\frac{C_{F,\Delta}}{\overline{C_{F,\Delta}}} = \frac{12}{5} \left(a' \bar{x}_{c_r}\right)^{1/2} \qquad \left(a' \bar{x}_{c_r} \geq 1\right) \tag{C11}$$

The value of a' over a range of wall temperature for both air and helium may be obtained from an integration of the results given in reference 22. These values are given in the following table, where T_w is an arbitrary but constant wall temperature and T_0 is the stagnation temperature since the analysis is based on a Prandtl number of 1, though as an approximation T_0 can probably be taken as the recovery temperature for Prandtl number $\neq 1$.

$\frac{T_w}{T_0}$	$\gamma = 1.4$		$\gamma = 1.67$	
	a'	$\bar{x}_0$	a'	$\bar{x}_0$
0	0.0983	10.17	0.1864	5.36
.2	.1769	5.65	.3531	2.83
.6	.3846	2.60	.8206	1.22
1.0	.6831	1.46	1.524	.656
2.0	[a]1.78	[a].562	4.200	.238

[a]From an extrapolation of the values given in reference 22.

A plot of the values of a' presented above is given in figure 16.

In the present case, for use with the delta-wing results presented in figure 12, the wings were assumed to be insulated; thus $a' = 0.68$ for air and $\bar{x}_0 = 1.46$. The maximum value of $\bar{x}_{c_r}$ for the delta wings used in the present experiments was about 0.35, so that equation (C10) with the third term neglected was used, or

$$C_{F,\Delta}\sqrt{R_{c_r}} = \overline{C_{F,\Delta}}\sqrt{R_{c_r}}\left(1 + 1.02\bar{x}_{c_r}\right) \tag{C12}$$

The value of $M_\infty{}^3\sqrt{C}$ was taken as 282 and $\overline{C_{F,\Delta}}\sqrt{R_{c_r}}$ as 1.64. The solution based on consideration of a reverse delta wing was assumed to hold for a delta wing flying point forward.

APPENDIX D

SKIN FRICTION OF A FLAT-PLATE DELTA WING WITH BOUNDARY-LAYER TRANSITION

This appendix is concerned with an evaluation of the skin friction on a flat-plate delta wing where a portion of the wing is covered by a turbulent boundary layer.

Effective Chord

The average skin-friction coefficient for a longitudinal element of a flat plate may be written $C_F \propto \frac{1}{c^{1/n}}$. If a triangular flat plate is being considered, with dimensions as shown in the sketch, the effective chord for purposes of determining the average skin friction for the entire plate is defined as

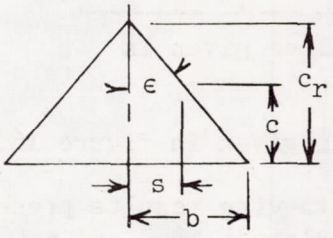

$$\bar{c} = \left(\frac{2}{bc_r} \int_0^b c^{\frac{n-1}{n}} \, ds \right)^{-n} \tag{D1}$$

Equation (D1) may be nondimensionalized by letting $s' = s/b$ and $c' = c/c_r$, and the result is

$$\frac{\bar{c}}{c_r} = \left[2 \int_0^1 (c')^{\frac{n-1}{n}} \, ds' \right]^{-n} \tag{D2}$$

Since $c' = 1 - s'$ equation (D2) may be readily integrated to obtain

$$\frac{\bar{c}}{c_r} = \left(\frac{2n - 1}{2n} \right)^n \tag{D3}$$

For various values of n, equation (D3) gives results as follows:

n	$\frac{\bar{c}}{c_r}$
2	0.5625
3	.5785
4	.5862
5	.5903
6	.5933
7	.5953

Consider now a triangular plate with a cutout, as shown in the following sketch:

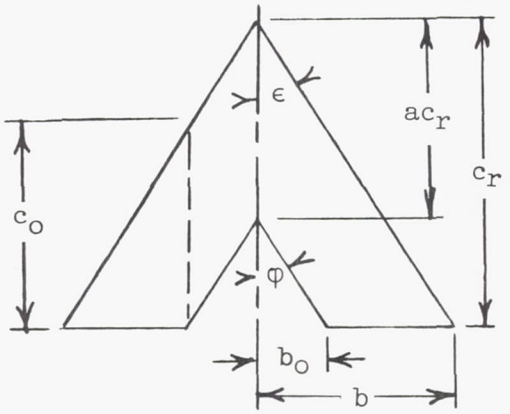

The effective chord in this case (where the skin-friction coefficient is based on the area of the wing without the cutout), when n = 2, is defined as

$$\bar{c} = \left(\frac{bc_r}{2}\right)^2\left(\int_0^{b_o} c^{1/2}ds + \int_{b_o}^{b} c^{1/2}ds\right)^{-2}$$

or, in nondimensional form,

$$\frac{\bar{c}}{c_r} = \frac{1}{4}\left[\int_0^{b_o/b} (c')^{1/2}ds' + \int_{b_o/b}^{1} (c')^{1/2}ds'\right]^{-2} \qquad (D4)$$

Substituting the variation of c with s into equation (D4) yields

$$\frac{\bar{c}}{c_r} = \frac{1}{4}\left\{\int_0^{b_o/b}\left[\frac{b}{b_o}\left(\frac{c_o}{c_r} - a\right)s' + a\right]^{1/2} ds' + \int_{b_o/b}^{1}\left[\frac{bc_o}{c_r(b - b_o)}(1 - s')\right]^{1/2} ds'\right\}^{-2} \tag{D5}$$

Equation (D5), upon integration, becomes

$$\frac{\bar{c}}{c_r} = \frac{9}{16}\left\{\frac{b_o}{b}\frac{1}{\frac{c_o}{c_r} - a}\left[\left(\frac{c_o}{c_r}\right)^{3/2} - a^{3/2}\right] + \left(1 - \frac{b_o}{b}\right)\left(\frac{c_o}{c_r}\right)^{1/2}\right\}^{-2} \tag{D6}$$

Equation (D6) is indeterminate when $\varphi = \epsilon$; however, it is a simple matter to reintegrate equation (D5) with this restriction, and the result is

$$\frac{\bar{c}}{c_r} = \frac{1}{4}\left[\sqrt{a}\left(1 - \frac{a}{3}\right)\right]^{-2} \tag{D7}$$

Laminar Skin Friction

For the flat plates considered in the preceding section an effective chord was defined in such a way that the average skin-friction coefficient for the entire plate could be written as

$$C_F = \frac{A}{\left(\frac{\rho_\infty u_\infty}{\mu_\infty}\bar{c}\right)^{1/2}}$$

When $n = 2$, substitution of equation (D7) gives

$$C_F = \frac{2A}{\left(\frac{\rho_\infty u_\infty}{\mu_\infty} c_r\right)^{1/2}}\sqrt{a}\left(1 - \frac{a}{3}\right) \tag{D8}$$

The ratio of the skin friction for the plate with the triangular cutout (where the edges of the cutout are parallel to the leading edges) to the skin friction of the complete triangular plate is as follows (from eq. (D8)):

$$\frac{F_c}{F_T} = \frac{3}{2}\sqrt{a}\left(1 - \frac{a}{3}\right) \tag{D9}$$

Skin Friction Due to Turbulent Boundary Layer

The cutout line is now assumed to represent instead the line along which instantaneous boundary-layer transition occurs. It is further assumed that transition occurs at a constant distance from the leading edge ($\varphi = \epsilon$).

As a basis for estimating the skin friction in the triangular region with turbulent flow, the momentum loss for the laminar boundary layer at the transition line is equated to the momentum loss for the turbulent boundary layer at the transition line. For a flat plate this is equivalent to a simultaneous solution of the equations for the momentum thickness. For the laminar boundary layer the momentum thickness may be represented by

$$\theta_a = \frac{A}{2}\left(\frac{ac_r\mu_\infty}{\rho_\infty u_\infty}\right)^{1/2} \tag{D10}$$

and for the turbulent boundary layer,

$$\theta_a = \frac{C}{2}\frac{m}{m-1}\frac{\left(\Delta x_T\right)^{(m-1)/m}}{\left(\frac{\rho_\infty u_\infty}{\mu_\infty}\right)^{1/m}} \tag{D11}$$

where Δx_T is the streamwise distance from the calculated start of the turbulent boundary layer at zero thickness to the point where transition occurs. The form of equation (D11) was actually obtained from consideration of the local skin-friction coefficient for turbulent flow in the form

$$C_f = C\left(\frac{\mu_\infty}{\rho_\infty u_\infty x}\right)^{1/m} \tag{D12}$$

Equating (D10) and (D11) gives

$$\Delta R_T = \left[\frac{A}{C}\frac{m-1}{m}\left(aR_{c_r}\right)^{1/2}\right]^{\frac{m}{m-1}} \tag{D13}$$

where ΔR_T is the Reynolds number from the calculated start of the turbulent boundary layer at zero thickness to the point where transition occurs, and R_{c_r} is the Reynolds number based on root-chord length.

Assuming that the average turbulent skin friction may be represented by an equation of the form

$$\Delta C_{F,turb} = \frac{D}{(\Delta R_T)^{1/q}} \tag{D14}$$

where q is the value of n obtained for the turbulent boundary layer. Then if the skin-friction coefficient is based on the total plan-form area of the triangular flat plate, substitution of equation (D13) into equation (D14) yields

$$\Delta C_{F,turb} = D(1-a)\frac{\left[\frac{A}{C}\frac{m-1}{m}\left(aR_{c_r}\right)^{1/2}\right]^{\frac{m}{m-1}\frac{q-1}{q}}}{R_{c_r}} \tag{D15}$$

The skin-friction coefficient that can be attributed to the area with turbulent boundary layer, including the imaginary area defined by ΔR_T, is, when based on the total plan-form area of the triangular flat plate,

$$C_{F,turb} = \frac{D}{\left[\Delta R_T + \xi(1-a)R_{c_r}\right]^{1/q}}(1-a)\frac{2\Delta R_T + (1-a)R_{c_r}}{R_{c_r}}$$

where ξ is a measure of the average chord in the region bounded by the lines for boundary-layer transition. When equation (D13) is substituted into this equation the result is

$$C_{F,turb} = \frac{D(1 - a)\left\{\frac{2\left[\frac{A}{C}\frac{m - 1}{m}\left(aR_{c_r}\right)^{1/2}\right]^{\frac{m}{m-1}}}{R_{c_r}} + (1 - a)\right\}}{\left\{\left[\frac{A}{C}\frac{m - 1}{m}\left(aR_{c_r}\right)^{1/2}\right]^{\frac{m}{m-1}} + \xi(1 - a)R_{c_r}\right\}^{1/q}} \tag{D16}$$

The average skin-friction coefficient for the triangular flat plate which is alined with the stream, with the assumptions of boundary-layer transition that have been made, is

$$C_F = \underbrace{\frac{4}{3}\frac{A}{\sqrt{R_{c_r}}}\frac{F_c}{F_T}}_{\text{Laminar}} + \underbrace{C_{F,turb} - \Delta C_{F,turb}}_{\text{Turbulent}} \tag{D17}$$

where F_c/F_T is given by equation (D9), $C_{F,turb}$ by equation (D16), and $\Delta C_{F,turb}$ by equation (D15).

Evaluation of Constants

A proper evaluation of the constants involved is the crux in determining accurate values for the average skin-friction coefficient by this method.

The constant A in equation (D17) may be evaluated from any of the available theories for the laminar boundary layer. For this report, the method given in reference 2 for hypersonic flow over an insulated plate with a Prandtl number of 1 was arbitrarily chosen. Equation (15) of reference 2 was, however, modified by the result of equation (D3) given here so that

$$C_F = \frac{4}{3}\frac{A}{\sqrt{\frac{\rho_\infty \mu_\infty}{\mu_\infty} c_r}} = \frac{4}{3}\frac{A}{\sqrt{R_{c_r}}} \tag{D18}$$

where

$$A = 2\sqrt{2\left(\frac{\theta}{\delta}\right)_\infty}(1 + k)^{3/4}\left(\frac{1 + \frac{\beta}{T_\infty}}{1 + k + \frac{\beta}{T_\infty}}\right)^{1/2}$$

$$k \equiv \frac{\gamma - 1}{2} M_\infty^2$$

and θ/δ is the ratio of the momentum thickness of the boundary layer to the total thickness of the boundary layer (linear velocity profile). Values of $(\theta/\delta)_\infty$ as a function of M_∞ are given in reference 2 or they can be obtained from the approximation

$$\left(\frac{\theta}{\delta}\right)_\infty \approx \frac{0.30685}{2 + k}$$

With the free-stream temperature T_∞ given in $^\circ R$, the Sutherland constant β has been taken as 177° F for hypersonic Mach numbers under ordinary wind-tunnel conditions. For lower supersonic Mach numbers and for flight conditions, the Sutherland constant may be taken as 198° F.

For the evaluation of the turbulent part of the skin friction, values must be determined for C, D, m, and q. To this end Van Driest's analysis for the turbulent boundary layer on a flat plate (ref. 26) was arbitrarily chosen; of course, there are other turbulent boundary-layer analyses which could as easily be utilized. The values of m and C were obtained by fitting equation (D12) in the range of Reynolds numbers desired to the values of local skin-friction coefficient obtained from equation (66) of reference 26. This equation is based on the power law for viscosity; however, for high temperatures where the variation of dynamic viscosity with temperature departs markedly from a power-law variation, it is a relatively simple matter to correct the exponent in the power law according to Sutherland's viscosity formula to obtain

$$\omega = \frac{3}{2} - \frac{\log_{10} \dfrac{T_w/T_\infty + \beta/T_\infty}{1 + \beta/T_\infty}}{\log_{10} \dfrac{T_w}{T_\infty}} \qquad \text{(D19)}$$

where ω is the exponent in the power law and T_w is the wall temperature. If the plate is insulated and the Prandtl number is 1, equation (D19) may be written as

$$\omega = \frac{3}{2} - \frac{\log_{10} \dfrac{1 + k + \beta/T_\infty}{1 + \beta/T_\infty}}{\log_{10} (1 + k)} \qquad \text{(D20)}$$

The values of D and q introduced in equation (D14) cannot, in this case, necessarily be found to the required accuracy from an integration of equation (D12). For the present computations, equation (79) (or eq. (77)) of reference 26 was used to obtain values to which equation (D14) was fitted over the desired range of Reynolds numbers.

A value must now be assigned to ξ. This constant is actually the ratio of the effective chord in the triangular region with turbulent boundary-layer flow to $(1 - a)c_r$. When $a = 0$, ΔR_T will also be zero and the value of ξ is that given by equation (D3) for the value of n $(=q)$ involved. A value of 0.55 was used for ξ in the computations for this report, since the turbulent boundary layer assumed does not start with zero thickness.

The remaining constants used were as follows: $A = 1.22$, $C = 0.125$, $D = 0.243$, $m = 3.27$, $q = 3.03$, $\omega = 0.86$, and values of a and R_{c_r} were assumed. The product aR_{c_r} (the transition Reynolds number) is designated as R_T in figure 15.

REFERENCES

1. Lees, Lester, and Probstein, Ronald F.: Hypersonic Viscous Flow Over a Flat Plate. Rep. No. 195, Princeton Univ., Aero. Eng. Lab., Apr. 20, 1952.

2. Bertram, Mitchel H.: An Approximate Method for Determining the Displacement Effects and Viscous Drag of Laminar Boundary Layers in Two-Dimensional Hypersonic Flow. NACA TN 2773, 1952.

3. Shen, Shan-Fu: An Estimate of Viscosity Effect on the Hypersonic Flow Over an Insulated Wedge. Jour. Math. and Phys., vol. XXXI, no. 3, Oct. 1952, pp. 192-205.

4. Li, Ting-Yi, and Nagamatsu, H. T.: Shock-Wave Effects on the Laminar Skin Friction of an Insulated Flat Plate at Hypersonic Speeds. Jour. Aero. Sci., vol. 20, no. 5, May 1953, pp. 345-355.

5. Stewartson, K.: On the Motion of a Flat Plate at High Speed in a Viscous Compressible Fluid - II. Steady Motion. Jour. Aero. Sci., vol. 22, no. 5, May 1955, pp. 303-309.

6. Lees, Lester: Hypersonic Flow. Fifth International Aeronautical Conference (Los Angeles, Calif., June 20-23, 1955), Inst. Aero. Sci., Inc., 1955, pp. 241-276.

7. Lees, Lester: Influence of the Leading-Edge Shock Wave on the Laminar Boundary Layer at Hypersonic Speeds. Jour. Aero. Sci., vol. 23, no. 6, June 1956, pp. 594-600, 612.

8. Kuo, Y. H.: Viscous Flow Along a Flat Plate Moving at High Supersonic Speeds. Jour. Aero. Sci., vol. 23, no. 2, Feb. 1956, pp. 125-136.

9. Pai, S. I., and Shen, S. F.: Hypersonic Viscous Flow Over a Wedge. Proc. Fourth Midwestern Conference on Fluid Mechanics, held at Purdue University September 8-9, 1955, Research Series No. 128, Purdue Engineering Experiment Station, pp. 259-272.

10. Bertram, Mitchel H.: Viscous and Leading-Edge Thickness Effects on the Pressures on the Surface of a Flat Plate in Hypersonic Flow. Jour. Aero. Sci. (Readers' Forum), vol. 21, no. 6, June 1954, pp. 430-431.

11. Kendall, James M., Jr.: An Experimental Investigation of Leading-Edge Shock-Wave - Boundary-Layer Interaction at Mach 5.8. Jour. Aero. Sci., vol. 24, no. 1, Jan. 1957, pp. 47-56.

12. Bogdonoff, Seymour M., and Hammitt, Andrew G.: Fluid Dynamic Effects at Speeds From M = 11 to 15. Jour. Aero. Sci., vol. 23, no. 2, Feb. 1956, pp. 108-116, 145. (See also: Hammitt, A. G., and Bogdonoff, S. M.: A Study of the Flow About Simple Bodies at Mach Numbers From 11 to 15. Rep. No. 277 (Contract AF 33(038)-250), Princeton Univ., Aero. Eng. Lab., Sept. 1954.)

13. Hammitt, A. G., and Bogdonoff, S. M.: Hypersonic Studies of the Leading Edge Effect on the Flow Over a Flat Plate. Jet Propulsion, vol. 26, no. 4, Apr. 1956, pp. 241-246, 250. (See also: Hammitt, A. G., Vas, I. E., and Bogdonoff, S. M.: Leading Edge Effects on the Flow Over a Flat Plate at Hypersonic Speeds. Rep. No. 326 (Contract AF 33(616)-2547), Princeton Univ., Dept. Aero. Eng., Sept. 1955.)

14. McLellan, Charles H., Williams, Thomas W., and Bertram, Mitchel H.: Investigation of a Two-Step Nozzle in the Langley 11-Inch Hypersonic Tunnel. NACA TN 2171, 1950.

15. McLellan, Charles H., Williams, Thomas W., and Beckwith, Ivan E.: Investigation of the Flow Through a Single-Stage Two-Dimensional Nozzle in the Langley 11-Inch Hypersonic Tunnel. NACA TN 2223, 1950.

16. Bertram, Mitchel H.: Exploratory Investigation of Boundary-Layer Transition on a Hollow Cylinder at a Mach Number of 6.9. NACA Rep. 1313, 1957. (Supersedes NACA TN 3546.)

17. McLellan, Charles H., Bertram, Mitchel H., and Moore, John A.: An Investigation of Four Wings of Square Plan Form at a Mach Number of 6.9 in the Langley 11-Inch Hypersonic Tunnel. NACA Rep. 1310, 1957. (Supersedes NACA RM L51D17.)

18. Ames Research Staff: Equations, Tables, and Charts for Compressible Flow. NACA Rep. 1135, 1953. (Supersedes NACA TN 1428.)

19. Von Kármán, Th.: The Problem of Resistance in Compressible Fluids. GALCIT Pub. No. 75, 1936. (From R. Accad. d'Italia, Cl. Sci. Fis., Mat. e Nat., vol. XIV, 1936.)

20. Eimer, M., and Nagamatsu, H. T.: Direct Measurement of Laminar Skin Friction at Hypersonic Speeds. GALCIT Memo. No. 16 (Contract No. DA-04-495-Ord-19), July 1, 1953.

21. Young, George B. W., and Janssen, Earl: The Compressible Boundary Layer. Jour. Aero. Sci., vol. 19, no. 4, Apr. 1952, pp. 229-236, 288.

22. Li, Ting-Yi, and Nagamatsu, H. T.: Hypersonic Viscous Flow on Noninsulated Flat Plate. Proc. Fourth Midwestern Conference on Fluid Mechanics, held at Purdue University September 8-9, 1955, Research Series No. 128, Purdue Engineering Experiment Station, pp. 273-287.

23. Chapman, Dean R., and Rubesin, Morris W.: Temperature and Velocity Profiles in the Compressible Laminar Boundary Layer With Arbitrary Distribution of Surface Temperature. Jour. Aero. Sci., vol. 16, no. 9, Sept. 1949, pp. 547-565.

24. Eggers, A. J., Jr.: One-Dimensional Flows of an Imperfect Diatomic Gas. NACA Rep. 959, 1950.

25. Roberts, J. K. (Rev. by A. R. Miller): Heat and Thermodynamics. Fourth ed., Blackie & Son, Ltd. (London and Glasgow), 1951.

26. Van Driest, E. R.: Turbulent Boundary Layer in Compressible Fluids. Jour. Aero. Sci., vol. 18, no. 3, Mar. 1951, pp. 145-160, 216.

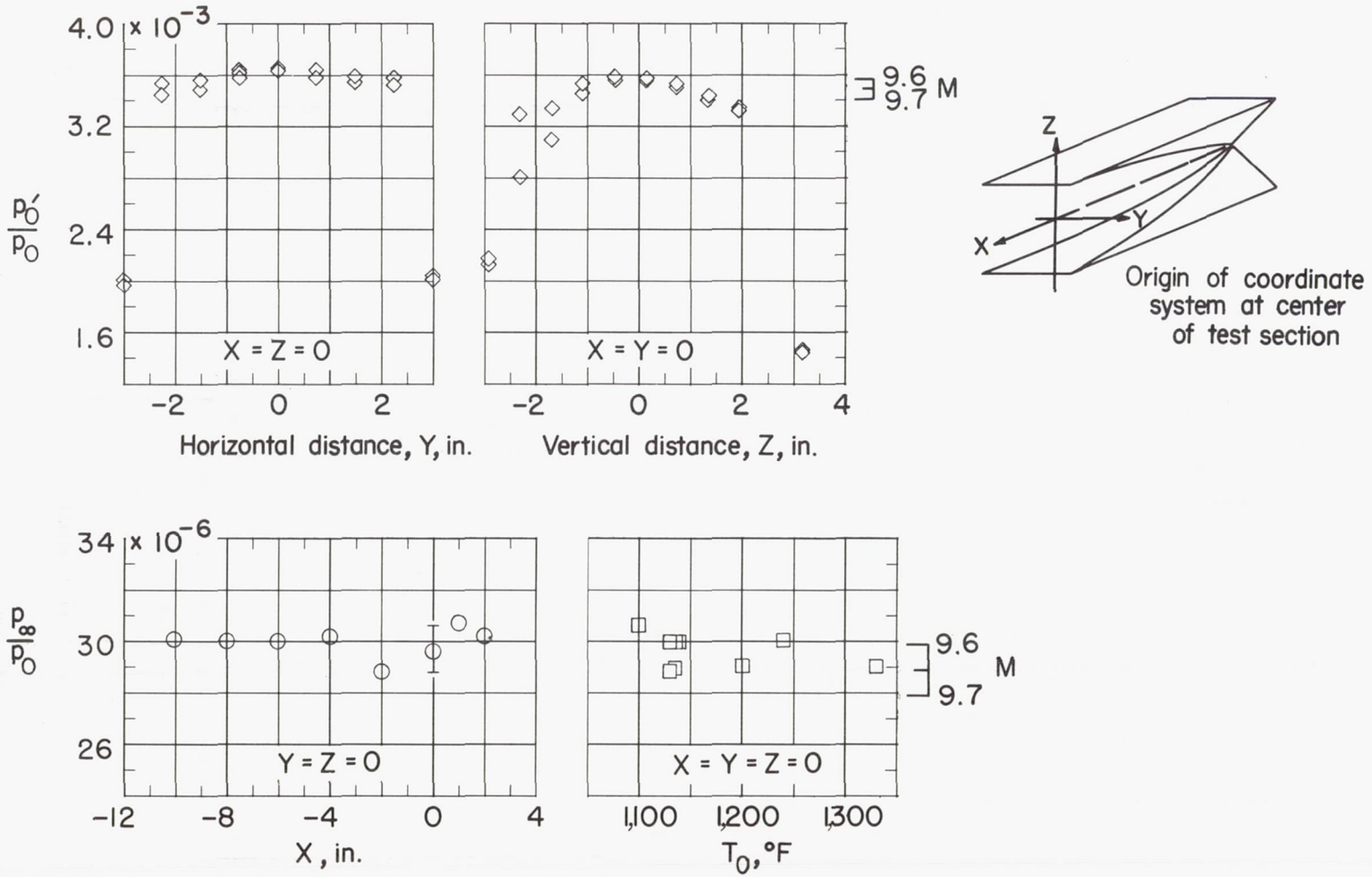

Figure 1.- Pressure distributions in the three-dimensional nozzle.

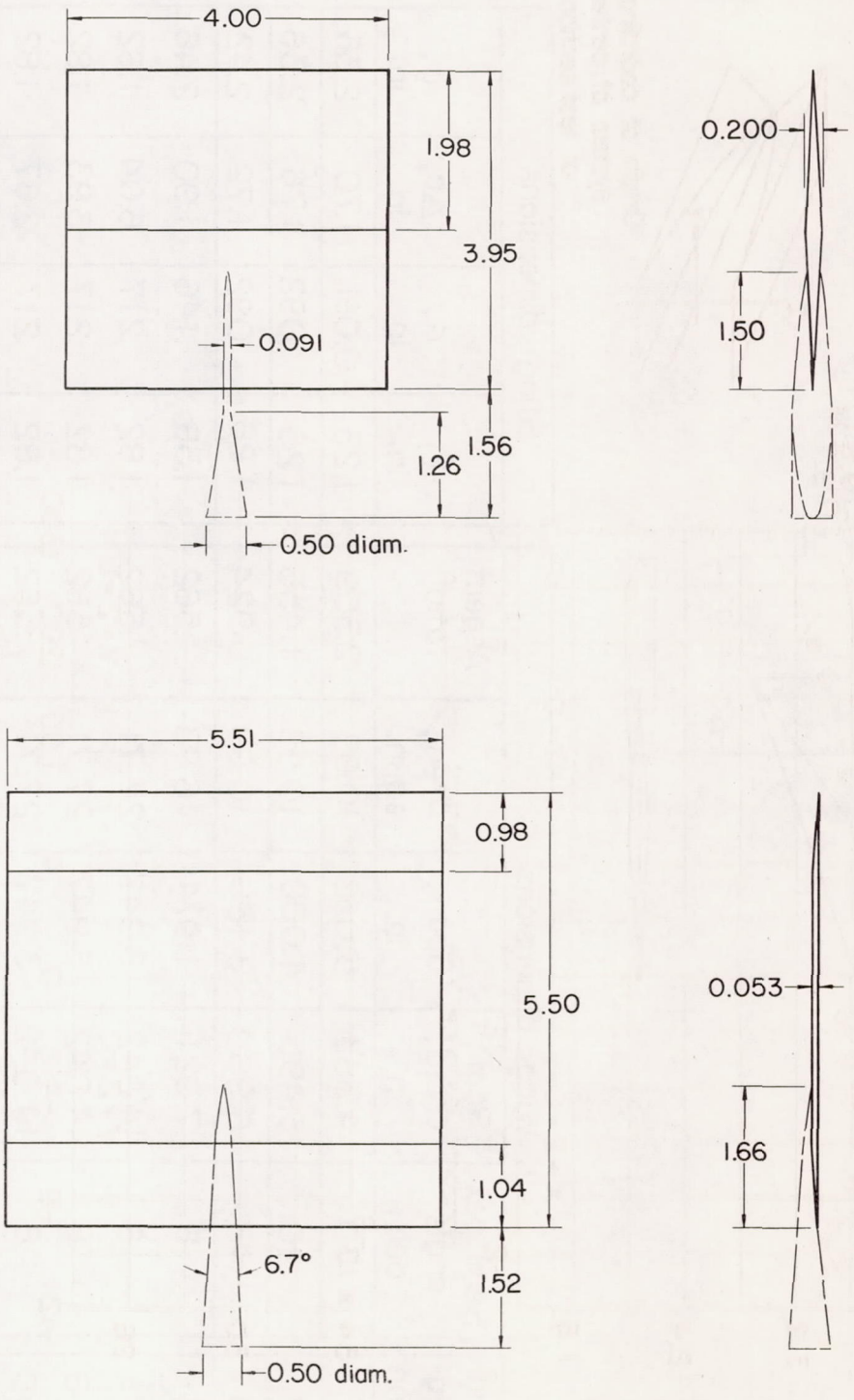

Figure 2.- Square-plan-form wings.

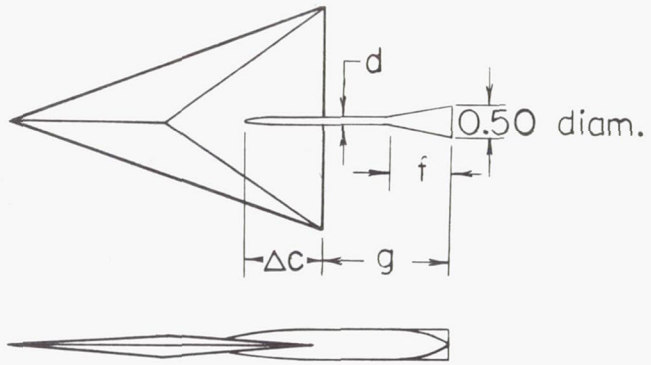

Wing designation	Wing dimensions					Sting dimensions			
	Semiapex angle, deg	Root chord, in.	Span, in.	Area, sq in.	Aspect ratio	f, in.	d, in.	Δc, in.	g, in.
1	30	4.363	5.038	10.99	2.309	1.23	0.091	1.70	2.36
2	20	5.495	4.000	10.99	1.456	1.25	.092	1.76	2.36
3	13	6.900	3.186	10.99	0.924	1.26	.092	1.72	2.42
4	8	7.021	1.974	6.93	.562	1.38	.146	1.90	2.46
4-A	8	14.042	3.947	27.71	.562	1.82	.217	6.04	1.82
4-B	8	14.042	3.947	27.71	.562	1.82	.217	3.93	1.82
4-C	8	14.042	3.947	27.71	.562	1.82	.217	2.67	1.82

Figure 3.- Delta wings.

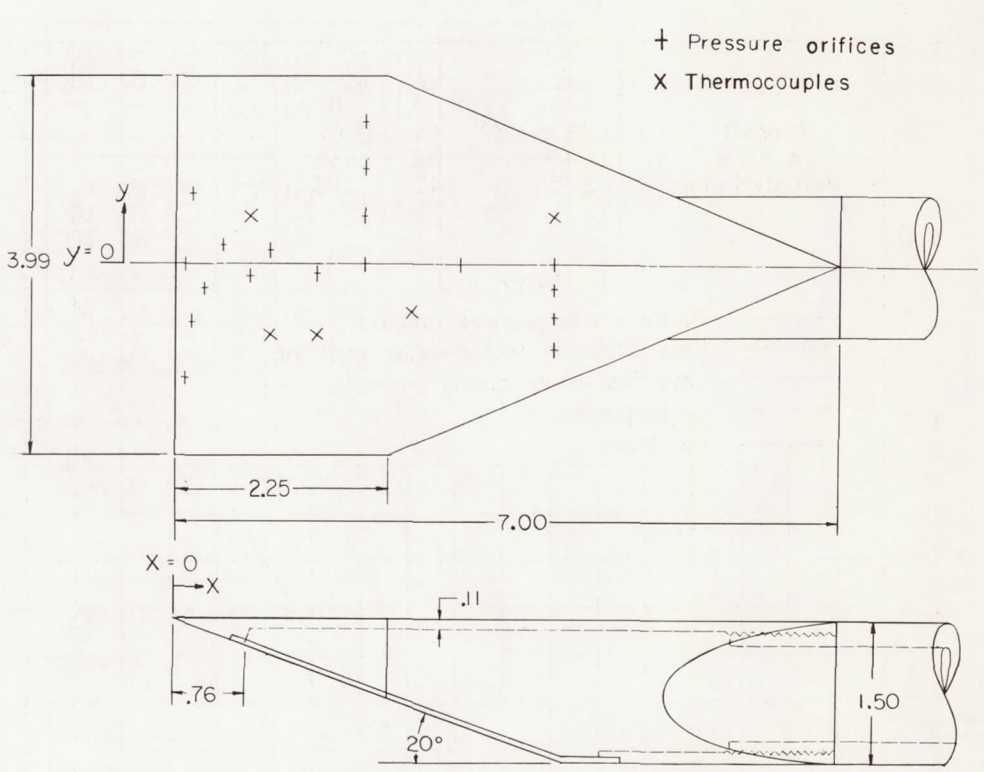

Pressure-Orifice Locations

x	y
.092	0
.089	-1.20
.161	.75
.164	-.59
.278	-.25
.480	.25
.737	-.12
.981	.15
1.482	-.09
1.978	0
1.978	.50
1.980	1.00
1.977	1.50
2.970	0
3.968	-.01
3.977	-.25
3.976	-.54
3.971	-.90

Thermocouple Locations

x	y
.76	.50
.95	-.73
1.45	-.74
2.46	-.50
3.85	.59

Figure 4.- Flat-plate pressure and temperature model.

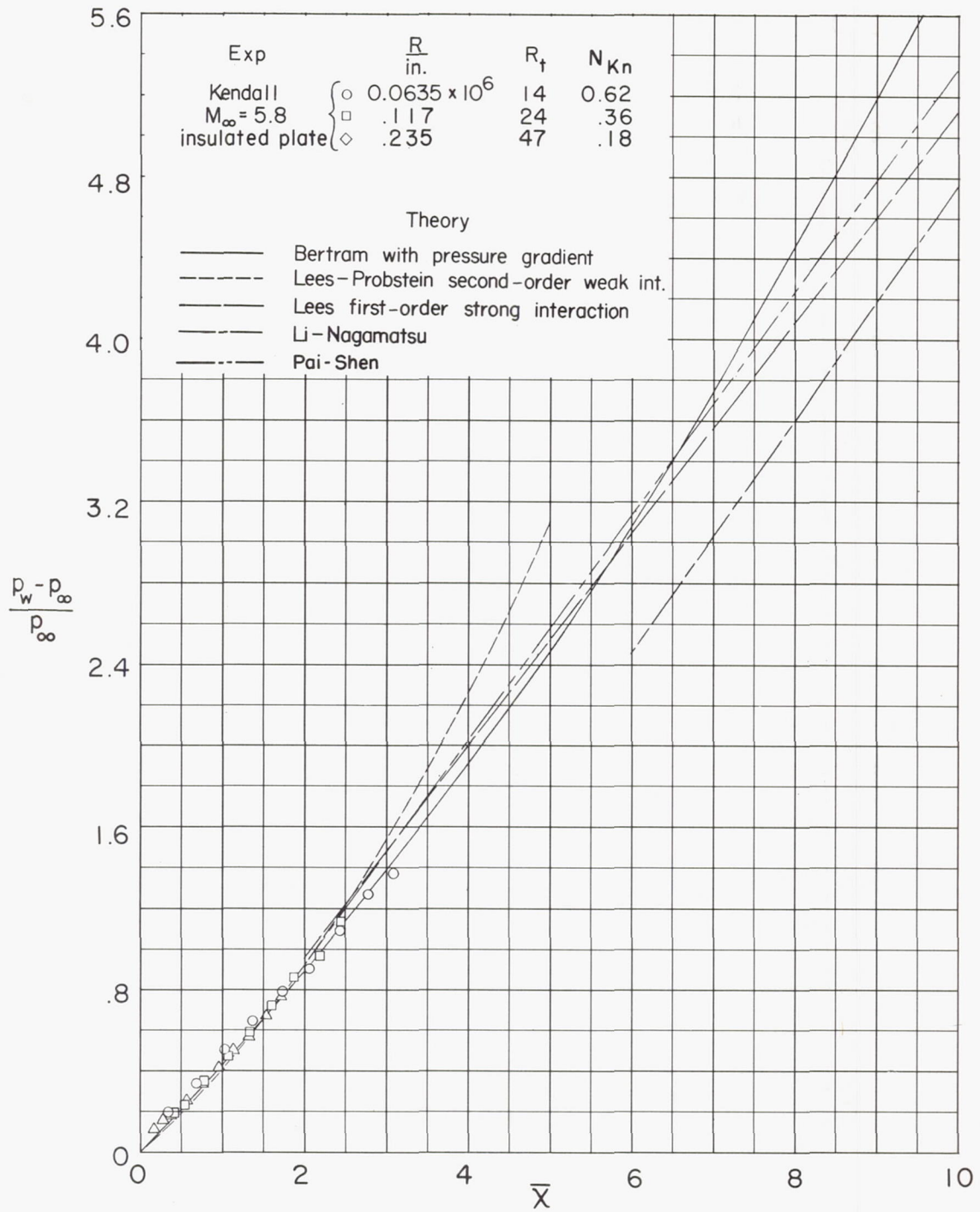

Figure 5.- Theories for predicting the induced-pressure effects on an insulated flat plate. $\gamma = 7/5$.

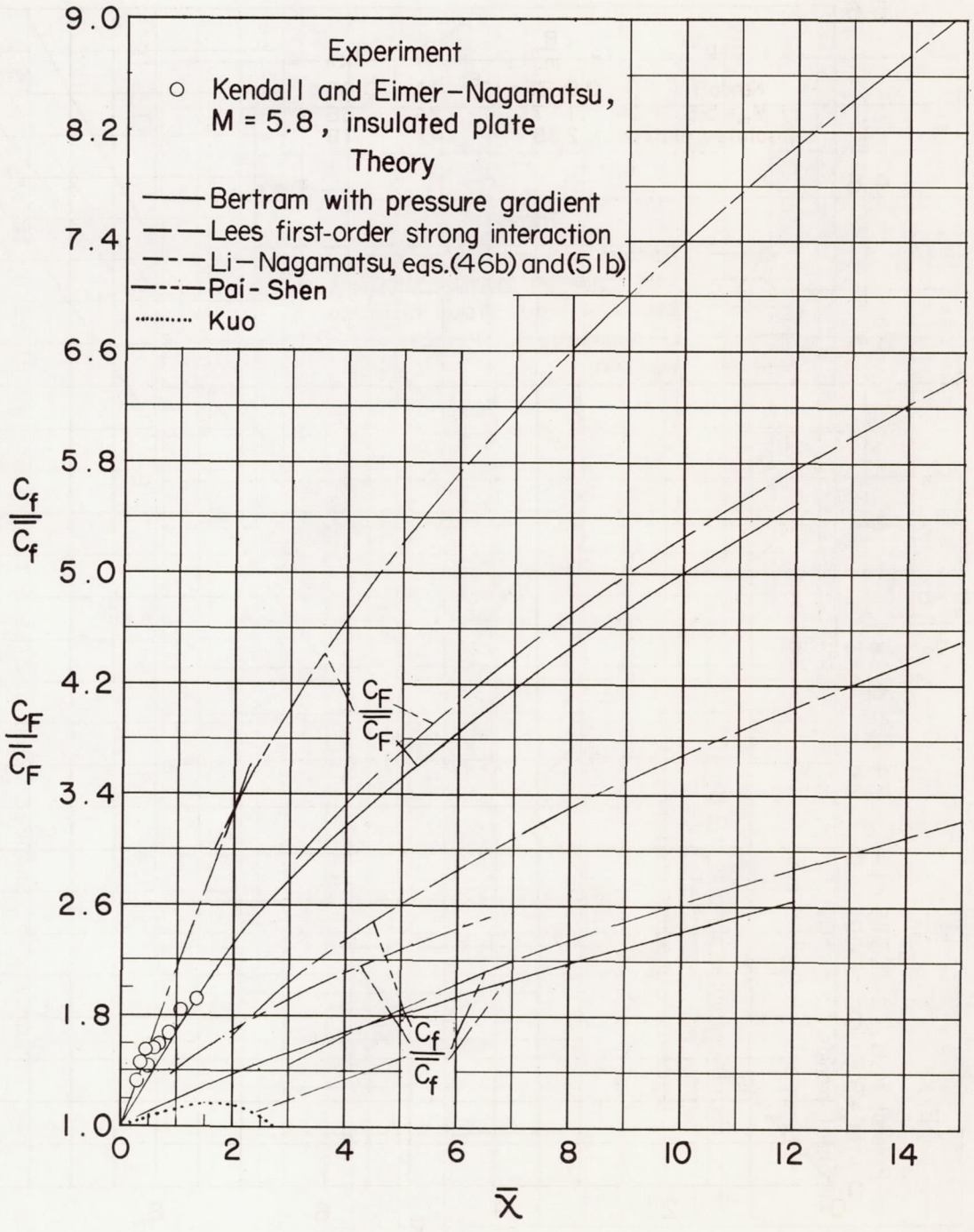

Figure 6.- Theories for predicting the induced-pressure effects on local and average skin-friction coefficients for an insulated flat plate. $\gamma = 7/5$.

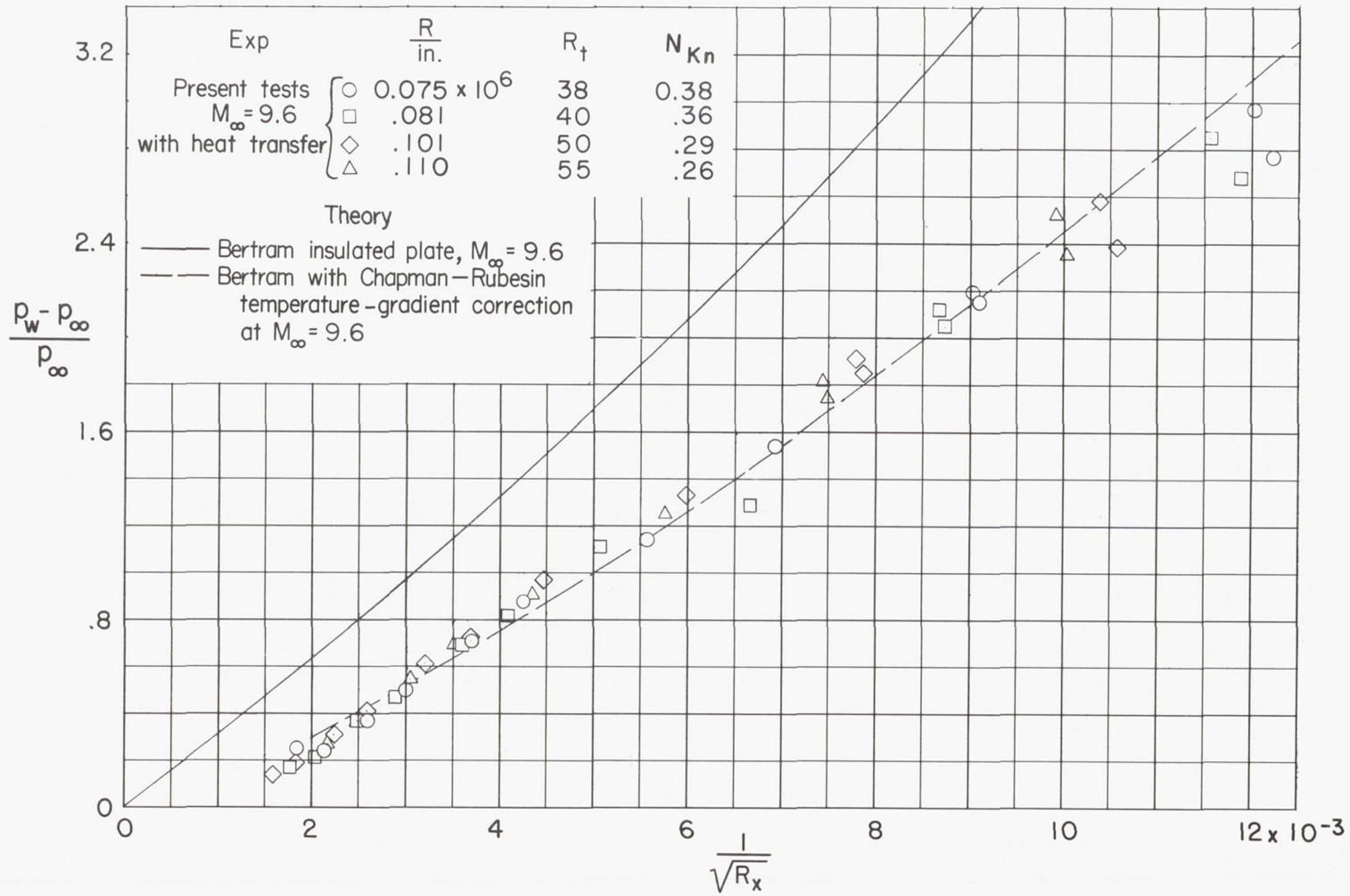

Figure 7.- Comparison of induced pressures on a flat plate as given by theory and by experiments in air at M = 9.6.

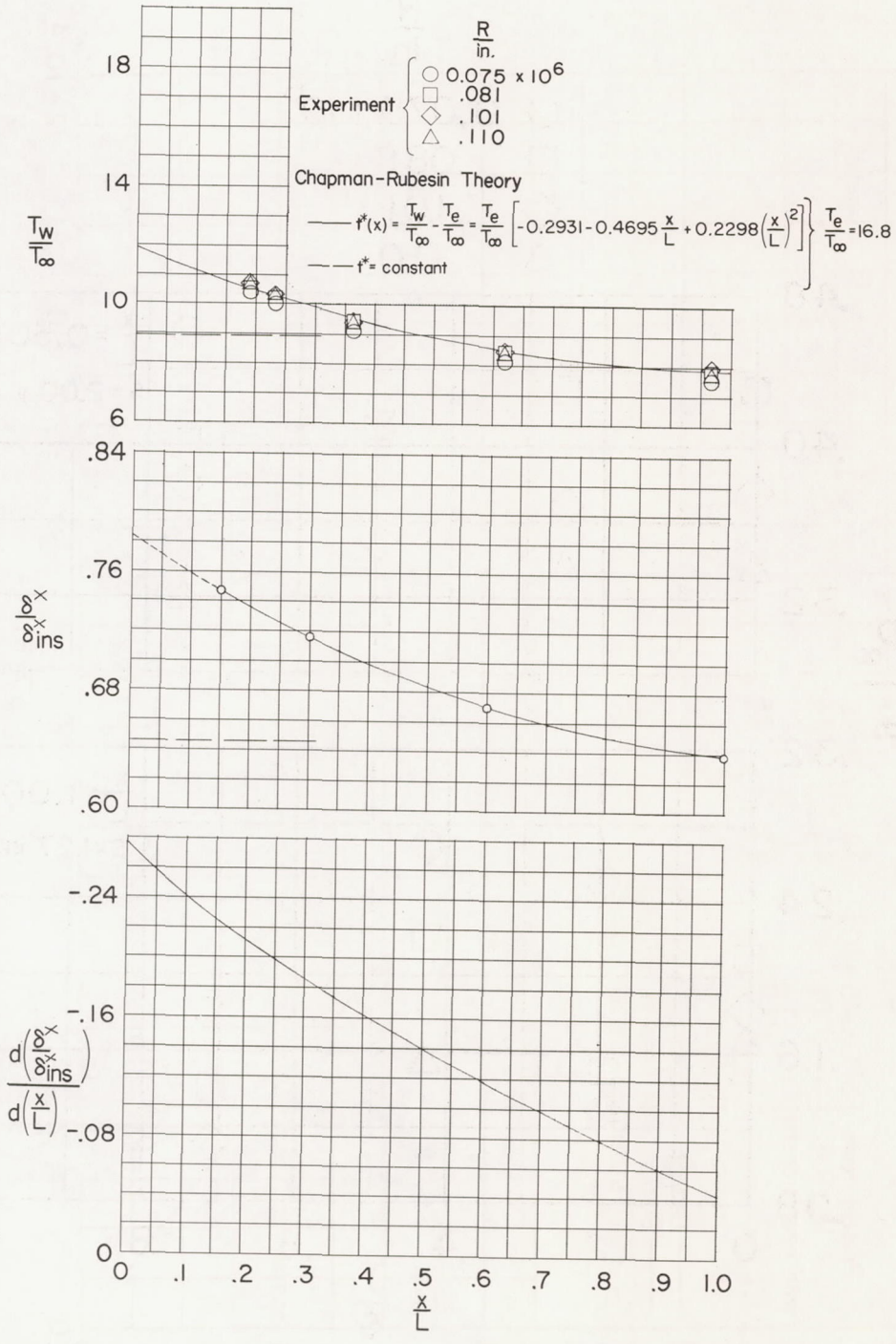

Figure 8.- Measured wall temperatures on pressure model and prediction of Chapman-Rubesin theory for the temperature effect on the displacement thickness. M = 9.6.

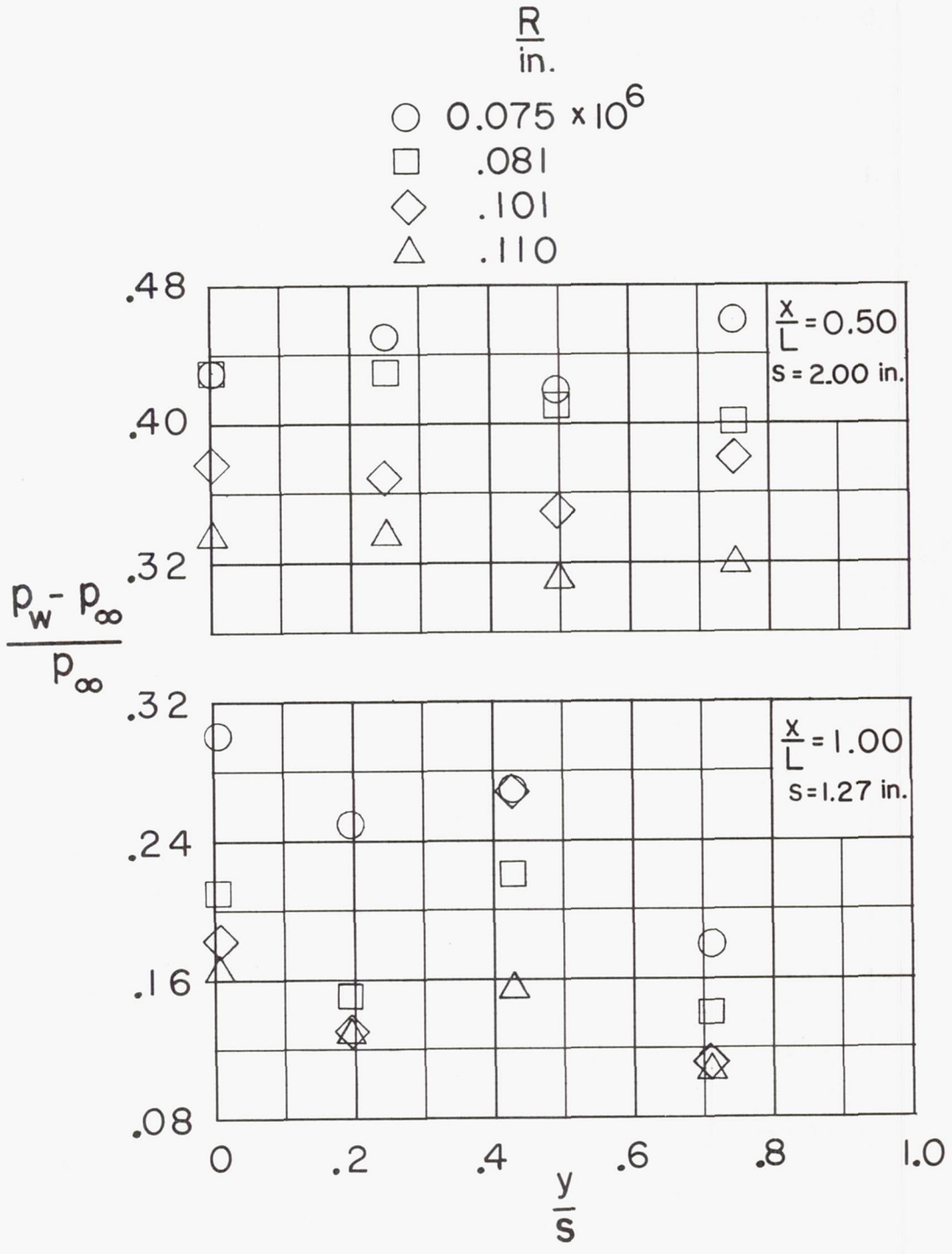

Figure 9.- Lateral distribution of pressure at two stations on flat plate. M = 9.6.

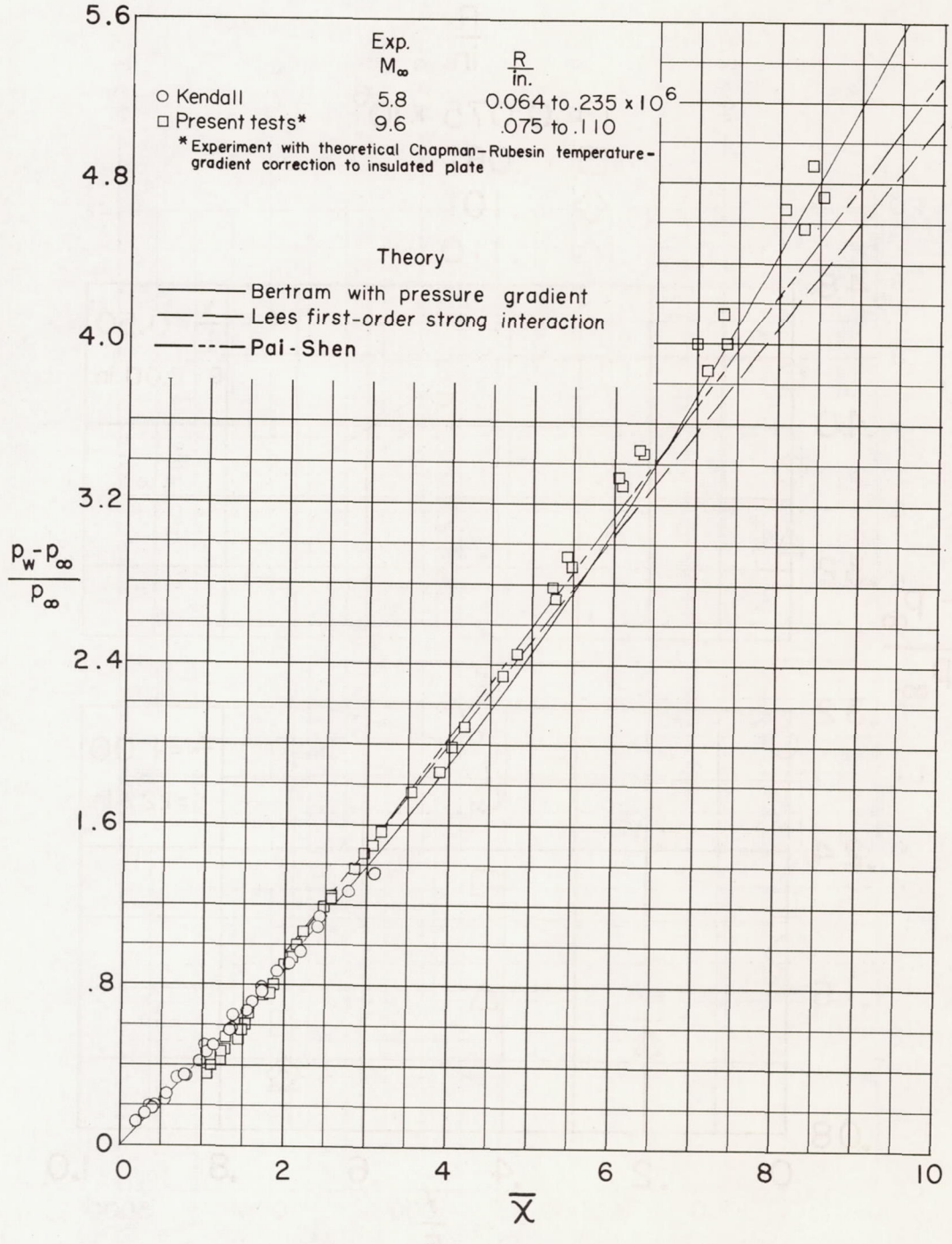

Figure 10.- Induced pressures on insulated flat plate. Data for M = 9.6 with heat transfer but corrected theoretically to insulated-plate case.

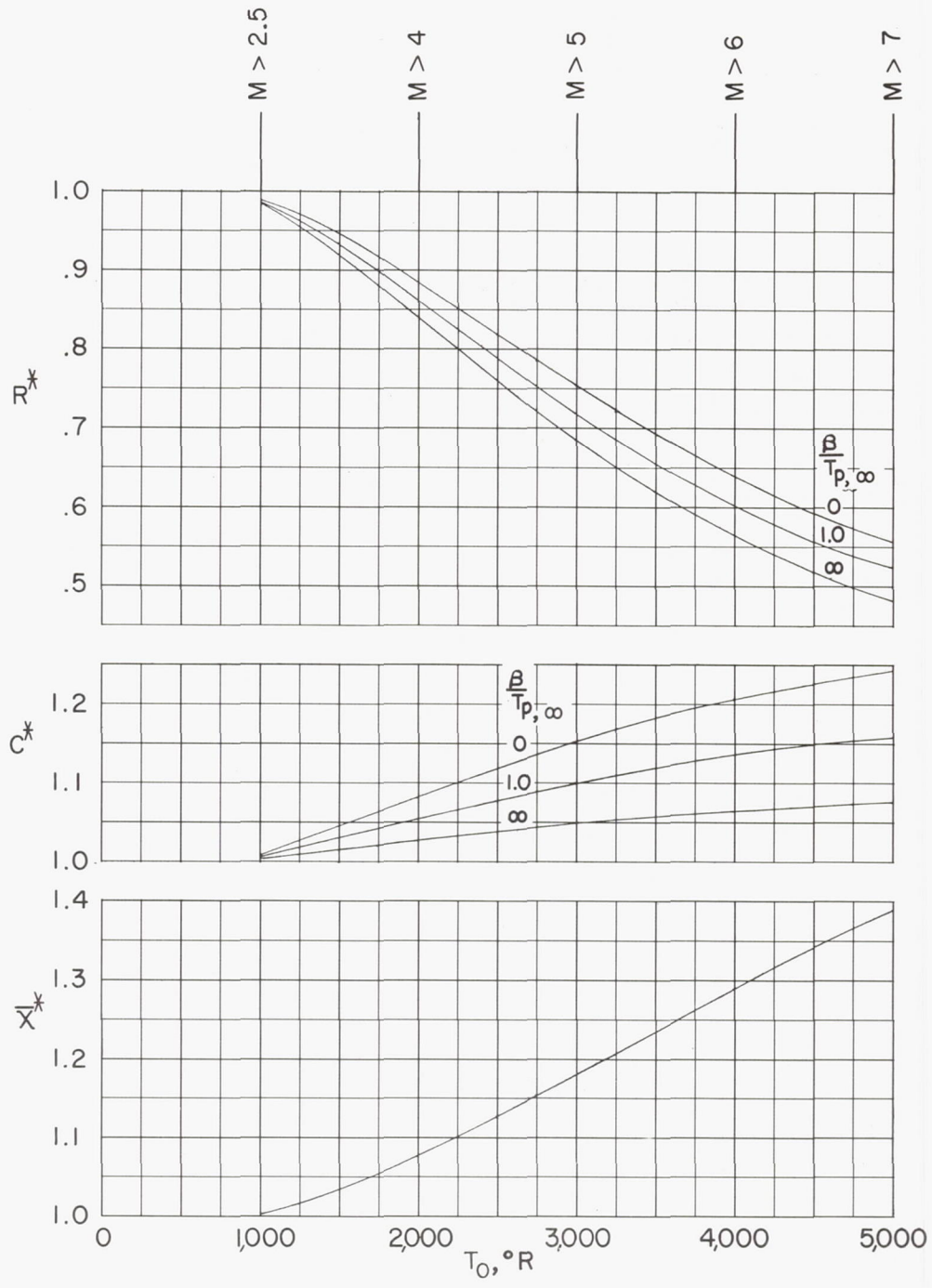

Figure 11.- Effect of caloric imperfections (variable γ) on Reynolds number, viscosity coefficient, and the viscous-interaction parameter.

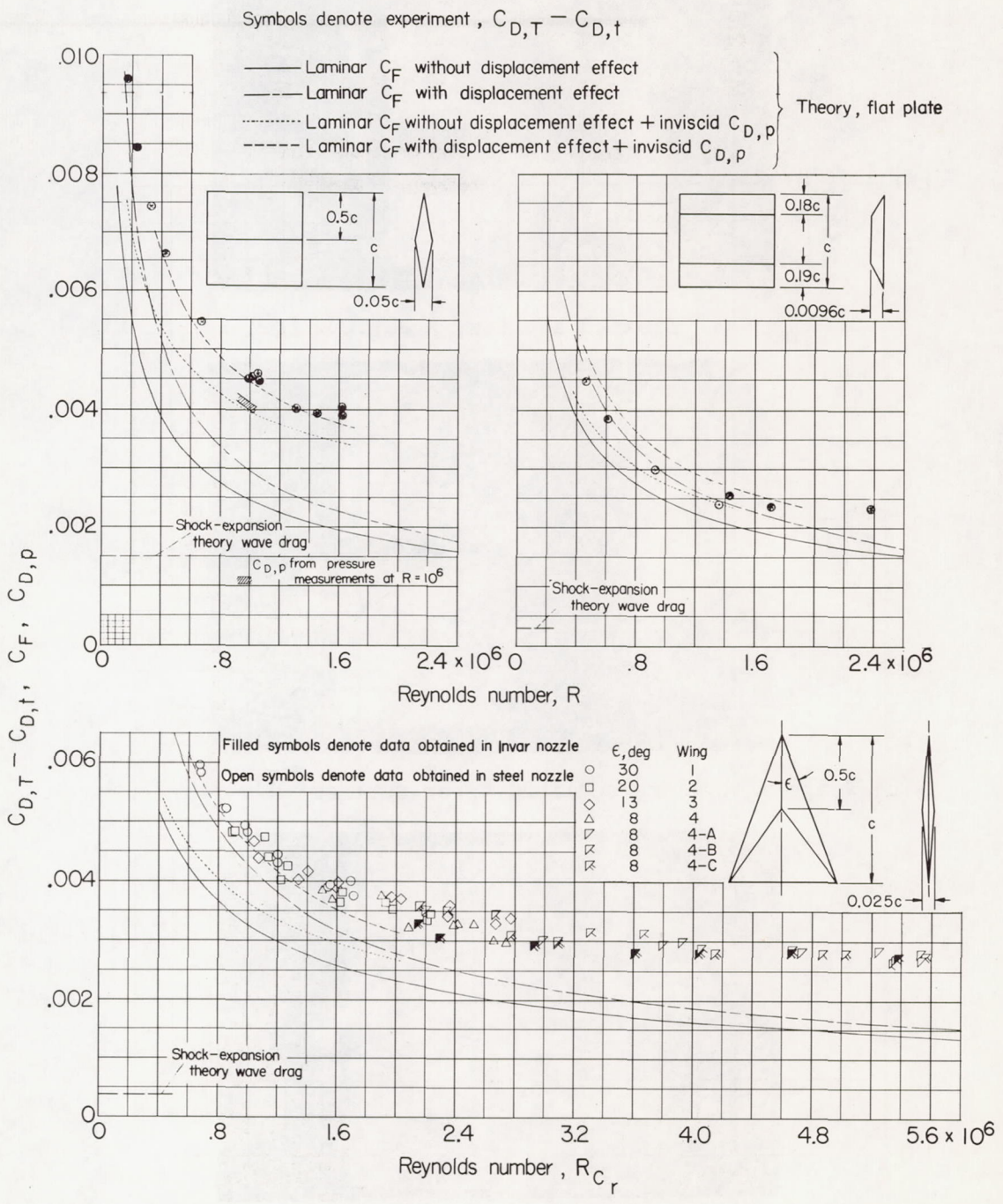

Figure 12.- Experimental and theoretical drag coefficients of square- and delta-plan-form wings.

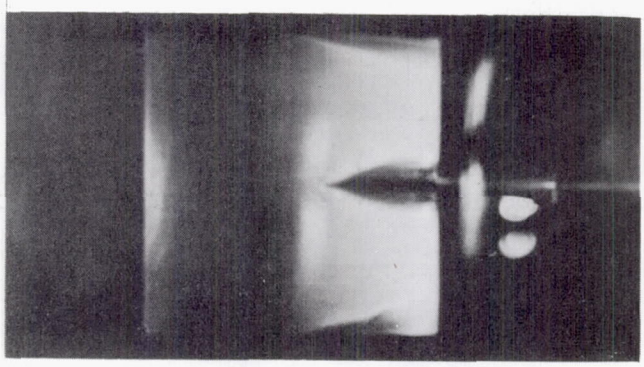

(a) Diamond section; $R = 1.2 \times 10^6$.

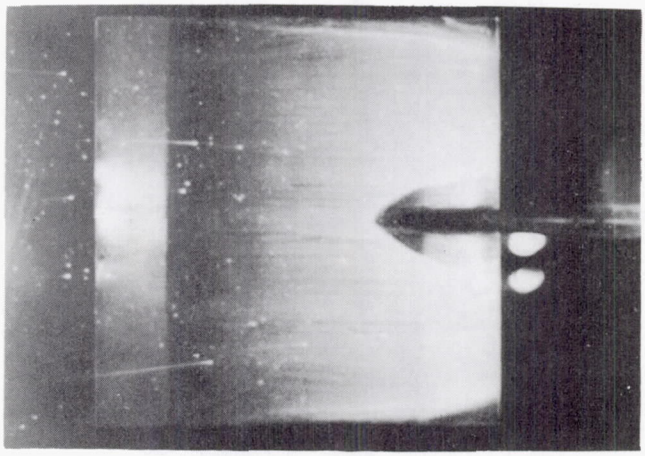

(b) Wedge-slab-wedge section; upper surface; $R = 1.7 \times 10^6$.

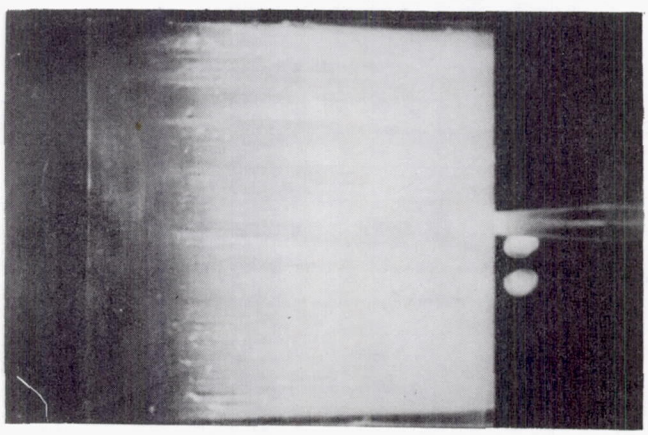

L-57-4437

(c) Wedge-slab-wedge section; lower surface; $R = 1.7 \times 10^6$.

Figure 13.- Surface oil-flow studies of the square-plan-form wings. $M = 6.9$.

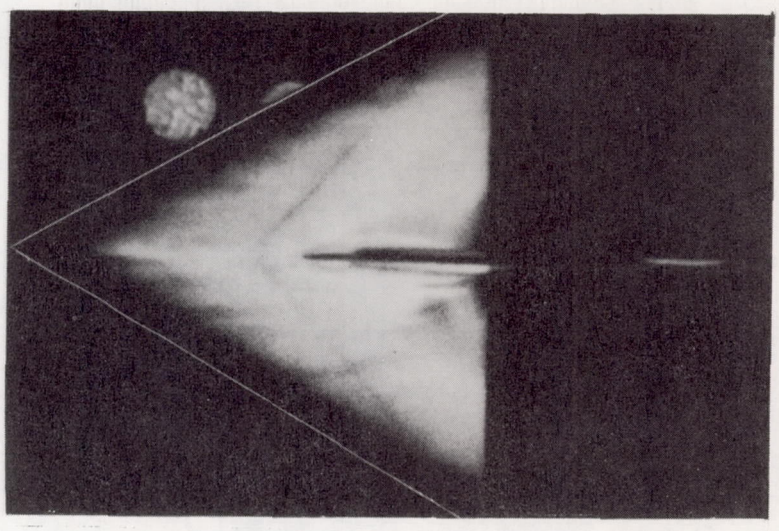

(a) Wing 1; $\epsilon = 30^{\circ}$; $R = 1.7 \times 10^{6}$.

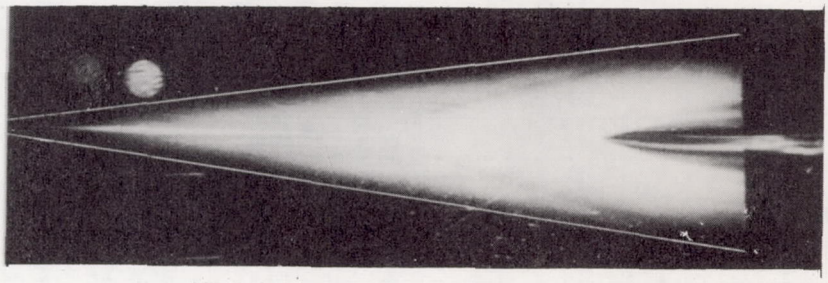

(b) Wing 4-C; $\epsilon = 8^{\circ}$; $R = 5.3 \times 10^{6}$.

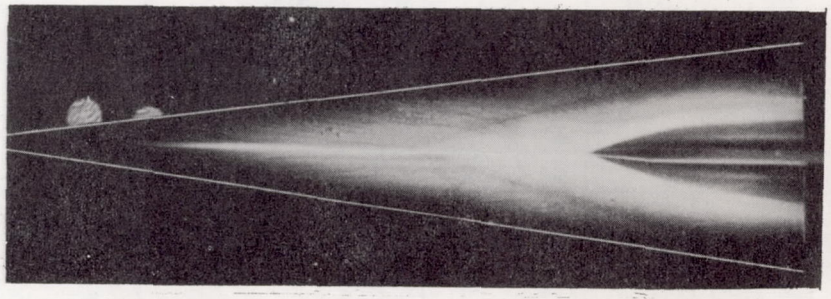

(c) Wing 4-B; $\epsilon = 8^{\circ}$; $R = 3.4 \times 10^{6}$. L-87898

Figure 14.- Surface oil-flow studies of two of the $2\frac{1}{2}$-percent-thick delta wings. M = 6.9. Lines have been added to indicate edges of wings, which were not visible in photographs.

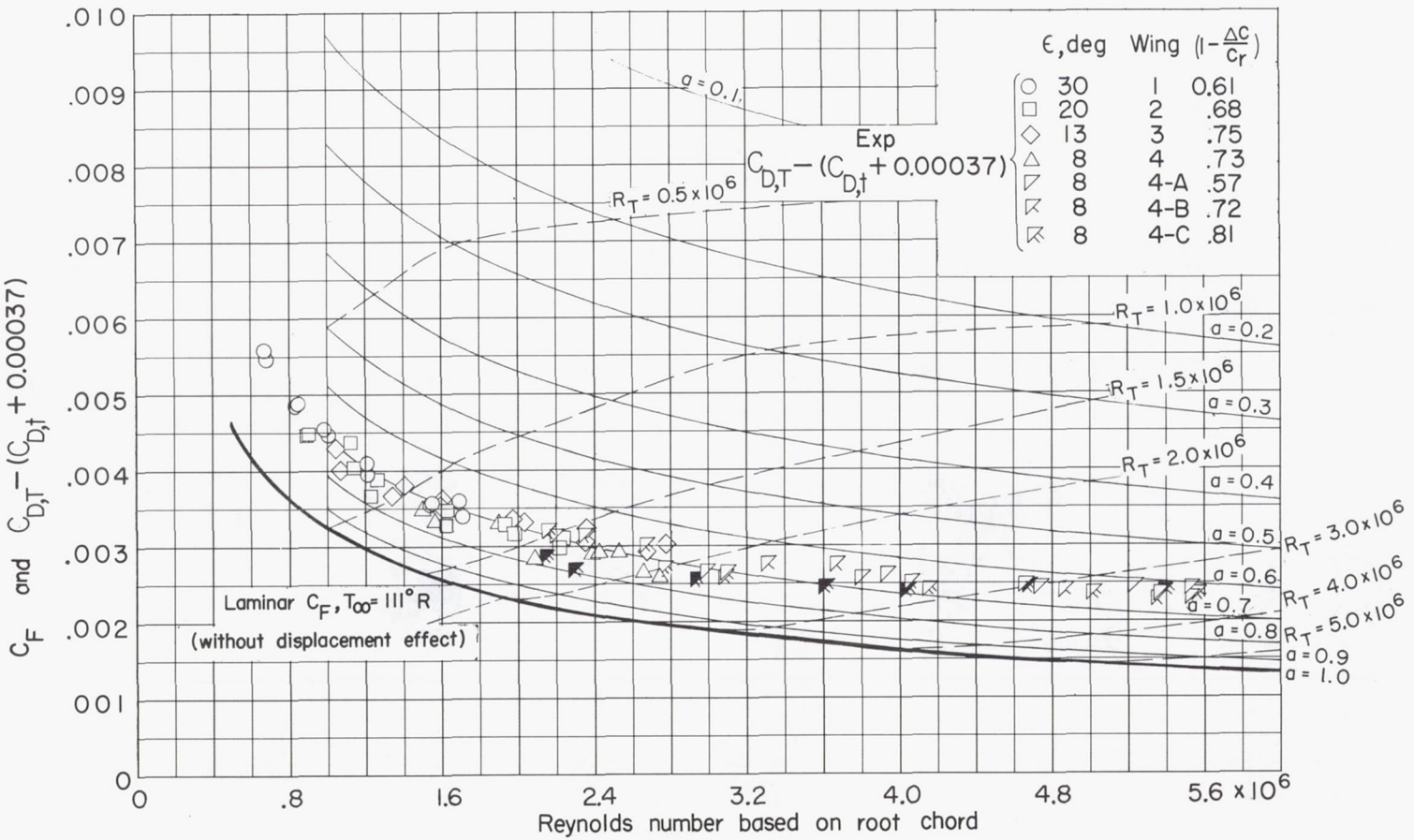

Figure 15.- Comparison of laminar and turbulent skin-friction coefficients with experiment. Experimental values are total drag from which an estimated leading-edge drag and pressure drag have been subtracted. M = 6.8. Open symbols denote data obtained in steel nozzle; solid symbols denote data obtained in Invar nozzle.

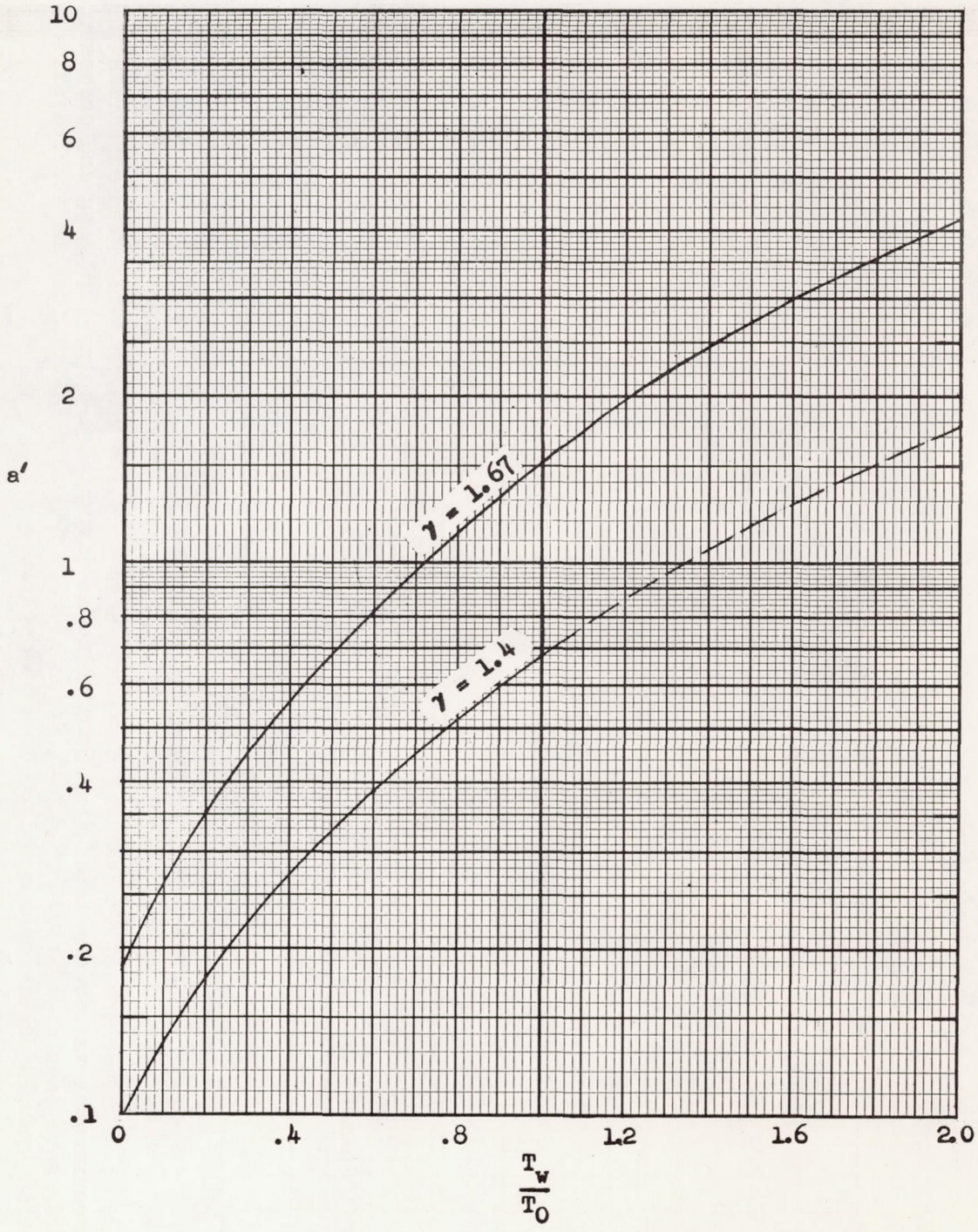

Figure 16.- Values of the coefficient a' in the equation for skin friction from viscous-interaction theory. See appendix C.